Holistic rockfall risk assessment in high mountain areas affected by seismic activity: Application to the Uspallata valley, Central Andes, Chile

Manon Farvacque, Nicolas Eckert, Gabriel Candia, Franck Bourrier, Christophe Corona, David Toe

Holistic rockfall risk assessment in high mountain areas affected by seismic activity: Application to the Uspallata valley, Central Andes, Chile

Manon Farvacque[1,2] | **Nicolas Eckert**[2] | **Gabriel Candia**[3,4] | **Franck Bourrier**[2] | **Christophe Corona**[1,5] | **David Toe**[2]

[1]Climate Change Impacts and Risks in the Anthropocene, Institute for Environmental Sciences, University of Geneva, Geneva, Switzerland

[2]Univ. Grenoble Alpes, INRAE, CNRS, IRD, Grenoble INP, IGE, Grenoble, France

[3]Facultad de Ingeniería, Universidad del Desarrollo, Las Condes, Santiago, Chile

[4]Research Center for Integrated Disaster Risk Management (CIGIDEN), ANID/FONDAP/15110017, Santiago, Chile

[5]Université Clermont Auvergne, CNRS, GEOLAB UMR, Clermont-Ferrand, France

Correspondence
Manon Farvacque, Climate Change Impacts and Risks in the Anthropocene, Institute for Environmental Sciences, University of Geneva, Bd. Carl-Vogt 66, CH-1205 Geneva, Switzerland.
Email: manon.farvacque@unige.ch

Abstract

Over large regions exposed to natural disasters, cascading effects resulting from complex or concatenated natural processes may represent a large portion of total risk. Populated high-mountain environments are a major concern, and methods for large-scale quantitative risk analyses are urgently required to improve risk mitigation. This article presents a comprehensive quantitative rockfall risk assessment over a large archetypal valley of the Andean mountains, in Central Chile, which integrates a wide spectrum of elements at risk. Risk is expressed as an expected damage both in monetary terms and casualties, at different scales relevant for decision making. Notably, total rockfall risk is divided into its main drivers, which allows quantifying seismically induced rockfall risk. For this purpose, the local seismic hazard is quantified and the yield acceleration, that is, acceleration required to initiate rockfall, is determined at the regional scale. The probability of failure is thereafter derived in terms of annual frequency of rockfall initiation and integrated in the quantitative risk assessment (QRA) process. Our results show the significant role of seismic activity as the triggering mechanism of rockfalls, and highlight elements at risk that have a major contribution to the total risk. Eventually a sensitivity analysis is conducted to (i) assess the robustness of obtained risk estimates to the data and modeling choices and (ii) identify the most influential assumptions. Our approach evidences the feasibility of large-scale QRAs in sensitive environments and opens perspectives for refining QRAs in similar territories significantly affected by cascading effects and multihazards.

KEYWORDS

cascading risks, central Andes, high mountain areas, large-scale analysis, quantitative risk assessment, rockfall risk, seismic risk

1 | INTRODUCTION

Critical infrastructure (e.g., industries, lifelines, housing, transport networks, energy, and water supply infrastructures) is essential for the functioning of a society and its economy. Over the years, these infrastructure have grown in interdependency and complexity. Hence, risks due to natural hazards increase rapidly due to the potential occurrence of disruptive events that affect large-scale territories (Serre & Heinzlef, 2018; Wang et al., 2011). Notably, large-scale areas often face a very wide range of natural hazards, and related risks include cascading risks (AghaKouchak et al., 2018) resulting from complex chains of processes that involve catastrophic interactions among different natural and technological hazards, with severe consequences to human lives, assets, and the environment (Zimmerman & Restrepo, 2009; Zuccaro et al., 2018).

From this perspective, mountain environments, especially at high elevations, appear as strongly sensitive. From a physical point of view, they are the place of extreme conditions (steep slopes, thaw-frost cycles, etc.) and they exhibit strong sensitivity to climate change (Pörtner et al., 2019). From a social point of view, they are often characterized by a high attractiveness, which generates a high real estate pressure

and, more widely, increases direct and indirect vulnerability, and, hence, casualties, and economic, environmental, and accessibility losses. This inherent complexity and changing nature make high mountain areas notoriously prone to multiple and cascading risks. Within this context, integrated large-scale quantitative risk analysis (QRA) accounting for the numerous factors at play are key elements for an effective and cost-efficient risk management, for example, Eckert and Giacona (2023).

QRA is indeed a relevant tool for stakeholders as it allows quantifying the risk in an objective and reproducible manner (Corominas et al., 2014; Farvacque et al., 2019b). However, in practice, the accurate quantitative estimation of the different components of risk is challenging (Corominas et al., 2005). In the specific field of rockfall risk, major limitations include the lack of knowledge regarding the vulnerability and both the exposure and economic value of the elements at risk (Ferrari et al., 2016), the limited number of well-documented case studies (Corominas et al., 2014; Ferrari et al., 2016; Volkwein et al., 2011), the rather limited spatial extension of the few available ones (in general a few hectares; Agliardi et al., 2009; Budetta et al., 2016; Corominas et al., 2005; Michoud et al., 2012; Guzzetti et al., 2004), and the nonexplicit consideration of the different triggering factors whose combination generates the total risk. This makes them often oversimplified with regard to reality. Specifically, methods to implement QRAs over large areas of high mountain environments affected by cascading processes are sorely lacking.

The Andean mountains, the longest mountain chain of the world and the second highest, is periodically affected by large magnitude earthquakes. Resulting ground motions can trigger several adverse events such as landslides and floods, and are considered as one of the main drivers of local rockfall activity (Stoffel et al., 2019). Losses directly related to earthquake hazard (e.g., collapse of buildings and failure of infrastructures) are increasingly well understood and quantified. However, indirect losses such as those due to rockfall triggered by this strong seismic activity remain much less known. Knowledge on the effect of seismic events on the occurrence of rockfalls has recently improved (Feng et al., 2019; Marzorati et al., 2002), notably from different techniques, such as optically stimulated luminescence (Kanari et al., 2019), dendrogeomorphology (Stoffel et al., 2019), terrestrial laser scanning (D'Amato et al., 2016), or seismic monitoring (DeRoin & McNutt, 2012), which allowed relating past rockfall activity to its drivers (e.g., earthquakes, weather events, volcanic activities). However, to our knowledge, these advances were not so far included within a rockfall QRA framework (Unterrader et al., 2018).

On this basis, the purpose of this article is to perform a comprehensive quantitative assessment of rockfall risk for a 50-km-long segment of the Uspallata valley, an archetypal valley of the Andean mountains in Central Chile where comprehensive QRAs are currently lacking. Our large-scale analysis originally integrates a wide spectrum of elements at risk, primarily the Route 60, a strategic road between Chile and Argentina, which is crucial for international trade, but also includes mining facilities, hydroelectric power plants, and buildings located at the vicinity of the road. We quantify risk, expressed in monetary terms and casualties, at different scales relevant for decision making. This evidences the added value of large-scale QRAs when it comes to identify hot spots where more detailed investigations and implementation of mitigation measures are crucial. Furthermore, we propose a framework that splits total rockfall risk as a function of its drivers. To this aim, we (i) computed the peak ground acceleration (PGA) seismic hazard at the 2.35 hm^2 cliff stretch located above a 200-m-long transect, (ii) determined the critical ground acceleration allowing to overcome the maximum resistance of the slope to sliding, that is, potentially inducing block motion, and (iii) derived the annual frequency of slope failure initiation due to regional seismic events. Also, as our approach involves summing-up a large amount of data and different models, a sensitivity analysis is conducted to (i) test the robustness of obtained risk estimates and (ii) identify the most influential choices. Finally, given the complexity of the considered risk system (large scale, different hazard drivers, a variety of the elements at risk, cascading processes, etc.), the QRA proposed in this research article is performed using the damage expectation. This risk measure, despite known drawbacks, has the advantage with regard to quantile-based risk measures of being (i) easier to handle for a complex system as ours and (ii) more known and accepted in the field of natural hazard to solve risk-based decision-making problems (Farvacque et al., 2021; Karlsson & Haimes, 1988). From this framework, we evaluate for the first time seismically induced rockfall risk in a quantitative way, which opens wide perspectives for refining QRAs in the numerous territories significantly affected by cascading risks, potentially on the basis of additional more advanced risk measures.

2 | STUDY AREA

The study area is a large portion of the Uspallata valley, located in the Central Andes mountains, east of Los Andes municipality, in the Valparaíso Region, Chile (Figures 1 and 2). This 50-km-long section extends from Los Chalets (1000 m a.s.l.) to the international tunnel Christ the Redeemer (3200 m a.s.l.) along the Aconcagua, Juncal, and Juncalillo rivers (Figure 2). The study area is encompassed by abrupt slopes made of highly fractured andesites and dacites from the Tertiary period (Figures 2B and 3A; Sernageomin, 2003). The cliff triggers rockfalls with sizes varying from gravel clasts to blocks larger than 20 m^3 (Figure 3B and C). The Andean mountains are affected by large earthquakes from Chile's subduction zone that are considered as one of the main driver of rockfall activity (Stoffel et al., 2019) in addition to shallow crustal seismicity. Additional factors related to, for example, meteorological conditions (Moreiras, 2006), also influence rockfall hazard in our study area. Fresh

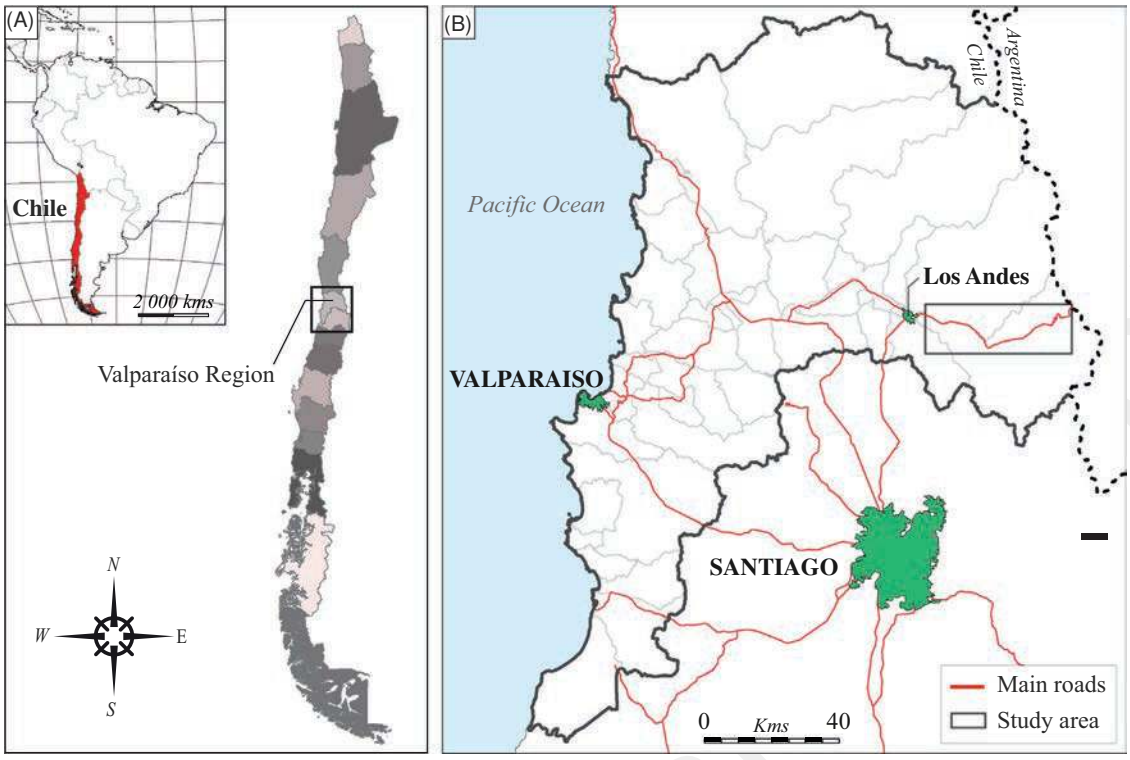

FIGURE 1 (A and B) The study area is located in Chile in the eastern part of the province of Los Andes, in Valparaíso Region, at the north-northeast of the city of Santiago.

blocks on the slope and testimonies from local security services further confirm ongoing strenuous rockfall activity and consequently the risk that it represents for local settlements and critical infrastructures.

From a socioeconomic perspective, the upper valleys of the Mendoza (in present-day Argentina) and Aconcagua rivers are of strategic importance as they provide a straight east–west path through the Andes. The use of the Uspallata valley to cross the Andean mountains dates back to the Inca empire, but its interest strongly increased during the colonial times as it provided the quickest and most direct route between Santiago de Chile and Buenos Aires (Fifer, 1994). Unfortunately, the elevation (3810 m a.s.l at Uspallata pass) and natural hazards (snow avalanches, rockfalls, and landslides) were making the crossing challenging. In 1873, to increase international trade and to secure the trips, the Clark brothers were commissioned the construction of a railroad, later know as the Transandine railway, which closely followed the ancient route used by travelers and mule-trains (Figure 2A; Purcell, 2007). Unfortunately, the repetitive delays or closures due to (i) damage on tracks and bridges by natural events, as well as (ii) the lack of coordination in train timetables, the Transandine railway closed in 1978–1979 (Fifer, 1991, 1994; Purcell, 2007). Simultaneously, as a result of the increased demand of ground transportation, Route 60 was constructed adjacent to the railroad line in the Chilean side (Figure 2A). This road is a dual track paved corridor including several snow shelters and a 3080-m-long tunnel in the Andes (at border between Chile–Argentina), better known as "Christ the Redeemer" tunnel (Figure 2A). Nowadays, the Uspallata road is the main transport route out of the Chilean capital city Santiago into Mendoza city in Argentina, resulting in an average traffic load of 1983 vehicles/day (i.e., one vehicle every 44 s; Centro Nacional de Investigación para la Gestión Integrada de Desastres Naturales CIGIDEN).

Moreover, the presence of natural resources reinforces the attractiveness of the region. On the Chilean side, the hydrological network allowed the creation of several hydroelectric plants (Figure 2A). South of Rio Blanco, mineral wealth led to the development of mining activities (Figure 2A) whose importance is attested by (1) the traffic of pick-ups used for mineral exploitation that represents 12% of the road No. 60 traffic while (2) the rail section of the Transandine railway has been reopened recently for the transport of mining materials from Rio Blanco to Los Andes (Figure 2A). Also, intense economic development has taken place along road No. 60 during the 20th century. Various infrastructures as well as settlements and dwellings for local populations have spread over the slopes, some of them being highly exposed to rockfall hazards. Eventually, even higher exposure to rockfall risk may be expected in the future due to further urban expansion, tourist development, and the possible restoration of the Transandine railway (Moreiras, 2006). By contrast, unfortunately, while snow sheds and deflection structures were implemented to prevent snow avalanches (Figure 2A), no mitigation plan currently exists to protect the various exposed stakes against rockfall events.

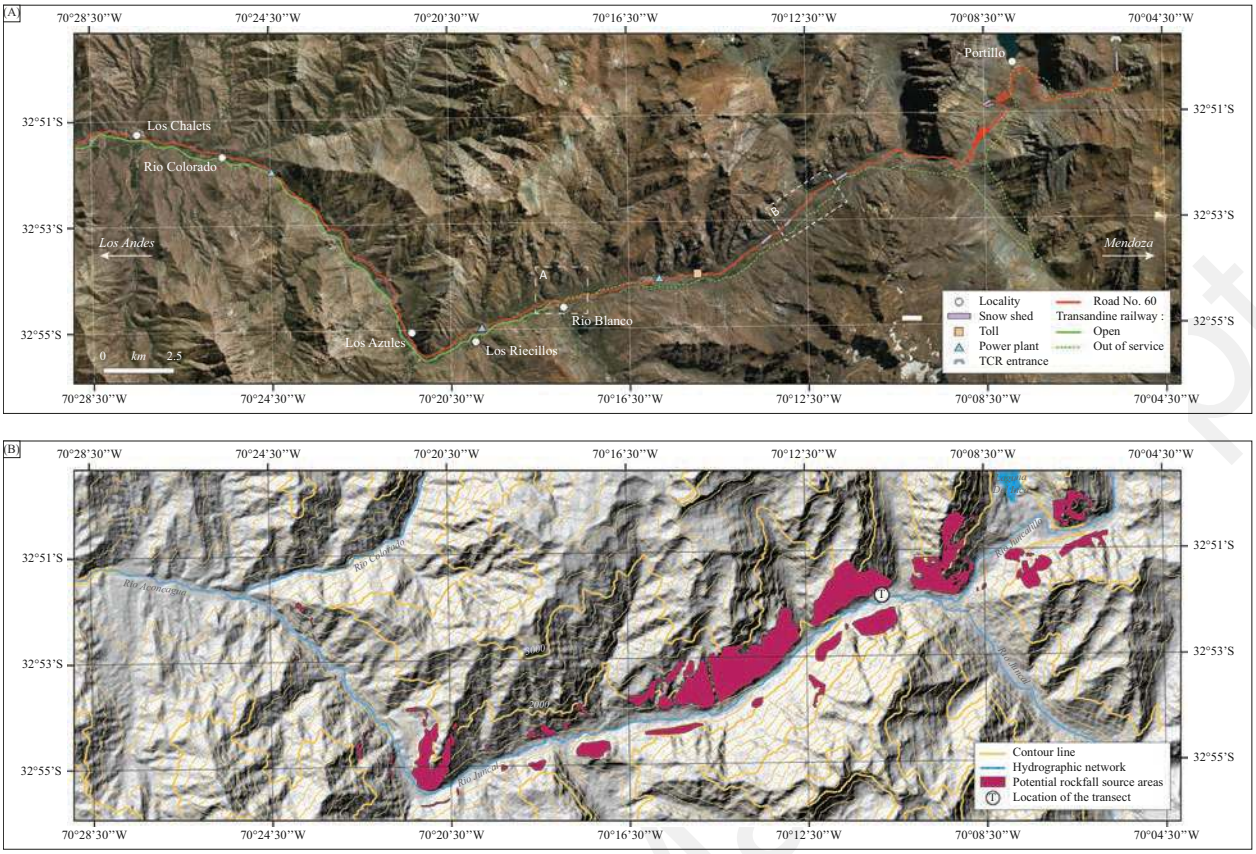

FIGURE 2 (A) The study area is located between 32°49'S–32°56'S and 70°28'W–70°04'W and extends 50 km from Los Chalets to the international tunnel Christ the Redeemer (TCR). (B) Geomorphological sketch of the study area highlighting potential rockfall source areas and location of the transect where block volumes have been inventoried.

3 | METHODS

3.1 | Quantitative risk evaluation

In analyzing risk, we are attempting to envision how the future will turn out if we undertake a certain course of action or inaction. Following Kaplan and Garrick (1981), the risk therefore corresponds to a list of outcomes or scenarios, described as:

$$(s_i, p_i, x_i), \tag{1}$$

where s_i is a scenario, and p_i as well as x_i the probability and the consequence of the scenario s_i, respectively. When plotting the (p_i, x_i) points by increasing severity and cumulative probability (see Kaplan & Garrick, 1981, for a detailed description), the risk is therefore represented though a curve well known as "risk curve." The mean of this risk curve, that is, the expected value (often an expected damage), is classically used to quantify risk. It has been widely used for risk assessments since it is intuitive and easy to compute. It also provides a suitable practical approach for comparing and aggregating risk, as it is based on a single number (Aven, 2009). Hence, in the field of rockfalls, the few studies, which so far performed QRAs almost exclusively adopted this risk measure (Agliardi et al., 2009; Corominas et al., 2019; Farvacque et al., 2019b; Moos et al., 2017; Mavrouli & Corominas, 2018).

However, the expected value/damage may be misleading since it does not properly capture the whole range of consequences, especially those related to rare events (Karlsson & Haimes, 1988; Yoshikawa & Goda, 2014). Alternative measures relying on the entire distribution of damages must therefore be promoted, as innovatively proposed in Farvacque et al. (2021) for rockfall risk analysis, where risk assessment is performed using quantile-based measures. Yet, given the variety of the elements at risk (punctual or linear) considered as well as the integration of different triggering factors, numerical difficulties to evaluate the damage distribution, and the extremely large size of the study area, the use of such risk measures is challenging in our case. Also, the expected damage remains better known and accepted by stake holders. As a consequence, we sticked at this stage on the expected damage as risk measure, as a first step to be expanded/supplemented in the future by other risk measures, see Section 6.4 for discussion.

3.1.1 | Total risk as expected damage

For rockfall, with the specific expected damage risk measure (Farvacque et al., 2021), risk is often expressed with the

FIGURE 3 (A) Fractured rock cliffs overhanging sections of road No. 60 and Transandine railway (〃 INRAE Grenoble). (B) Rockfall event that occurred in 2012 at road No. 60 toll (〃 Ministerio de Obras Públicas, Gobierno de Chile). (C) Recent small boulders on the side of road No. 60 (INRAE Grenoble).

following generic integral formulation:

$$\overline{R}_w = \sum_{z \in w} Z_w \times q(z_w) \times \lambda \times p_z \int p_z(Event) \times d_z(Event)\, dEvent, \quad (2)$$

where $\overline{R}_w$ represents the expectations of the consequences (or a certain amount of damage) of hazard activity for the whole system at risk, w (Farvacque et al., 2019a, 2020). This system is composed of a set of any element or combination of elements z potentially at risk, characterized by an exposure factor $q(z_w)$ and a value Z_w (physical quantity, economic value, etc.). In the most common configurations, these elements are physical (i.e., people, traffic infrastructure, buildings), but other less tangible aspects can potentially be introduced such as the image and aesthetics of an element. λ is the temporal rate of occurrence of potentially damageable events (e.g., measured in events/year). Integration is performed over the variability of rockfall events. The latter is related to different physical and kinematic properties, that is, volume, mass, shape, translational and rotational energies, passing height, impact angle, and so forth from one rockfall to another. In addition, the damage expectation is evaluated considering only rockfall events that reach the element z. Hence, p_z is the reach probability on the element at risk z, $p_z(Event)$ the local distribution of physical and kinematic properties of rockfall events reaching z, and $d_z(Event)$ the resulting damage. Depending on the purpose of the analysis, the damage can refer, for example, to a failure probability for buildings and infrastructures (physical vulnerability) or casualties (vulnerability of people). Based on vulnerability

curves (Cappabianca et al., 2008; Corominas et al., 2014; Favier et al., 2014, 2018), the damage level is expressed on a scale ranging from 0 (no damage) to 1 (total damage).

Finally, due to the complexity and suddenness of rockfall processes, several parameters (e.g., fragmentation of the block, impact angle) that would be useful for risk assessment are systematically lacking (Bourrier et al., 2016). As a consequence, in practice, kinetic energy is generally the sole magnitude variable considered within the risk quantification. This leads the following simplified equation:

$$\overline{\mathrm{R}}_w = \sum_{z \in w} Z_w \times q(z_w) \times \lambda \times p_z \int p_z(E) \times d_z(E)\, \mathrm{d}E, \quad (3)$$

where $p_z(E)$ is the local distribution of kinetic energy E conditional to reach and $d_z(E)$ the resulting damage.

3.1.2 | Separation of total risk as function of triggering factors

When rockfall activity is related to different triggering factors (e.g., rainfalls, earthquakes, freeze–thaw events, snow and ice melt), assessing the contribution of each of these to total rockfall risk may be useful. Assuming one single triggering factor per rockfall event and using the law of total probabilities, total rockfall risk can be easily separated as a sum of the risk due to each triggering factor as:

$$\overline{\mathrm{R}}_w = \sum_{z \in w} Z_w \times q(z_w) \left(\sum_{j=1}^{n} \lambda_{\mathrm{T}_j} \times p_{z_j} \int p_{z_j}(E) \times d_z(E)\, \mathrm{d}E \right) \quad (4)$$

$$= \sum_{j=1}^{n} \overline{\mathrm{R}}_w(\mathrm{T}_j), \quad (5)$$

with $\sum_{j=1}^{n} \lambda_{\mathrm{T}_j} = \lambda$. p_{z_j} is the reach probability on the element at risk z for triggering factor j and $p_{z_j}(E)$ is the local distribution of kinetic energy E conditional to reach and triggering factor j. Note that $d_z(E)$ is independent of T_j as it only depends on E.

3.2 | Determination of elementary risk components

Rockfall risk assessment involves four main steps: (1) analysis of rockfall activity in order to quantify the temporal occurrence of events and their associated volume distribution, (2) modeling of rockfall trajectories to account for the spatially distributed nature of the rockfall process, (3) evaluating the probability for a given element at risk to be at the impact location at the time of impact, (4) assessing damages suffered due to rockfall impacts by making use of vulnerability curves. Finally, the required risk estimates are derived from the resulting damage distribution. In practice, it involves many assumptions. Most critical ones are synthesized in Table 1, and a sensitivity analysis is conducted to investigate to w hich extent they affect risk estimates.

3.2.1 | Rockfall probability

Rockfall phenomena start by the detachment of blocks from their original position (Crosta & Agliardi, 2003) and consequently, QRA must be performed by including all potential release areas. The simplest empirical approaches identify rockfall sources from field observations, expert judgments, historical data, or theoretical assumptions (Corona et al., 2013; Frattini et al., 2008; Guzzetti et al., 2003; Li et al., 2019; Toppe, 1987). Nowadays, recent technologies involving photogrammetry (Budetta et al., 2016) or LiDAR (light detection and ranging) surveying method (D'Amato et al., 2016; Macciotta et al., 2015; Strunden et al., 2015) allow detecting discontinuities within a structure with high-quality resolutions. Similarly, increasing availability of both digital elevation models (DEMs) and geographic information systems (GIS) lead to a rapid detection of potential rockfall sources based on slope angles statistics (Loye et al., 2009; Michoud et al., 2012).

Furthermore, the temporal probability of failure must be addressed to define the probability of the occurrence of a rockfall event, expressed in terms of frequencies or return periods (Ferrari et al., 2016). The most common approach for evaluating the hazard frequency involves the retro-analysis of past events. In that respect, the analysis of site-specific inventories provides the mean number of events that occur within a period of time (Ferrari et al., 2016).

Yet, as rockfall events can be initiated for different sizes of block, rockfall frequency assessment must consider a wide range of volumes. Statistical modeling of extreme values has now emerged as an important statistical discipline that aims at generically quantifying the stochastic behaviour of extreme events (Coles, 2001). Here, we adopted an asymptotic model from the generalized Pareto distribution (GPD) family to characterize the distribution of volumes exceeding a volume threshold value u. According to Pickands (1975), for any random variable, this is the true limiting distribution as soon as u is high enough. Following this approach, the cumulative rockfall volume distribution is given by:

$$\Pr\left\{ V > v \mid V > u \right\} = \left[1 + \xi \left(\frac{v-u}{\sigma} \right) \right]^{-1/\xi}, \quad (6)$$

where V represents the volume of the blocks (in m^3) and u, σ, and ξ, the location, scale, and shape of the GPD distribution, respectively. This approach focuses on (rather) large rock volumes, those whose distribution can be assessed on the field and that represent a significant threat (blocks with very low volumes do not propagate far enough and/or do not have a kinetic energy high enough to damage assets located downslope).

TABLE 1 Summary of some critical assumptions (in bold) involved in the QRA implementation. Other choices regarding rockfall initiation and propagation models, vulnerability of the different considered elements at risk to rockfall, the choice of the expected damage as risk measure, etc. are discussed in the text.

Risk component	Assumption	Justification	Direct impact on
Magnitude of seismic activity (Section 3.3.1)	Earthquake recurrence follows a **Poisson process**	Reasonable approximation for small to medium earthquakes; Standard assumption in PSHA	Hazard
Total rockfall frequency (Section 4.2.1)	Reference period for the computation of rockfall frequency of **10,000 years**	End of last glacial period; absence of more precise dating of rockfall events	Hazard
Rockfall frequency from seismic and meteorological triggers (Section 4.2.2)	Slope failure within a rock wall leads to the detachment of **one individual rock mass**	No strong support in scientific literature of alternative assumptions	Hazard
Rockfall volume distribution from seismic and meteorological triggers (Section 4.3.2)	**Seismic activity** is the preferential trigger for **large rockfall events** (D1); **Meteorological conditions only trigger** rockfall **within the 0.5 m^3 to 1.5 m^3 range** (D2)	Local expertise on process activity, no support in scientific literature of alternative assumptions	Hazard
Rockfall propagation (Section 4.4)	**No rock fragmentation**	Classical assumption in rockfall trajectory simulations, feasibility of large-scale computations	Hazard
Rockfall propagation (Section 4.4)	Regardless impact energy, the resistance of buildings to rockfalls is **infinite**, so that simulations reaching buildings are stopped, while the resistance of vehicles is set to **zero**, so that simulations impacting a vehicle continue propagating	No information or support in scientific literature providing better estimates	Hazard
Rockfall damage (Section 4.4)	For vehicles, the damaging value **regardless impact energies is set to 1**	No damage assessment of vehicles exposed to rockfalls	Damage
Exposure of moving elements at risk (Section 4.5)	The traffic is **uniformly distributed** in space and time	No precise information on local traffic variations	Exposure

3.2.2 | Rockfall propagation

Due to the scattering of the rockfall phenomenon, the propagation component must also be taken into account in rockfall hazard assessments (Crosta & Agliardi, 2003). Rockfall trajectories are modeled in this study using the Rockyfor3D (v5.0) code (Dorren, 2012). This probabilistic process-based rockfall trajectory model combines physically based deterministic algorithms with stochastic approaches to simulate rockfall in three dimensions. The model calculates sequences of classical, uniformly accelerated parabolic free fall through the air and rebounds on the slope surface and trees (for details, see Dorren et al., 2005). As outputs, the model provides, for example, information on rock propagation for any location in the study area, the number of rocks passing through a given surface, or the mean of the maximum kinetic energy values of all simulated blocks at a given location.

In the transit area, Rockyfor3D uses a normal and a tangential coefficient of restitution to calculate rock rebound on the slope surface (Volkwein et al., 2011). The normal coefficient of restitution (r_n) defines the change in normal velocity during impact. In Rockyfor3D, r_n values are associated with slope materials depending on mechanical properties, that is, the capacity of slope materials to dissipate energy. The tangential coefficient of restitution (r_t) defines the reduction in tangential velocity during impact. Both coefficients depend on: (i) the rock shape and radius and (ii) the depth of the impact crater during a rebound (Dorren, 2012). The parameters adopted to characterize interactions between the block and the soil—soil mechanical properties (i.e., restitution coefficients) and soil roughness—were described by the land-use and land-cover (LULC) patchiness (Farvacque et al., 2019a).

3.2.3 | Rockfall damage and exposure

This study aims at assessing rockfall risk for a wide spectrum of elements at risk, including structural elements (building type) and moving vehicles. The degree of loss suffered by an element at risk due to a rockfall impact is evaluated by making use of so-called vulnerability curves (Corominas et al., 2014). For structural elements, energies recorded over the Rockyfor3D simulations are expressed in terms of damage value based on the physical vulnerability curve proposed by Agliardi et al. (2009), where the potential damage varies between 0 (no structural damage) and 1 (total collapse) as:

$$d(E) = 1 - \frac{1.358}{1 + e^{\frac{E-129000}{120300}}}, \quad (7)$$

where d represents the damage suffered by a building to a rockfall impact of energy E (in Joules).

Regarding vehicles, the physical vulnerability refers to the damage suffered by the vehicle cabin due to rockfall impact. According to Bunce et al. (1997), a rock with sufficient energy to deform the road pavement could destroy a vehicle. In that case, the degree of loss of a vehicle impacted by a rockfall event is inexorably 1.

Finally, quantification of exposure mainly depends on the type of element potentially exposed (Corominas et al., 2014). Indeed, there is an important distinction between static (e.g., buildings, utilities, or traffic infrastructure) and moving (e.g., vehicles, trains, people) objects. Disregarding impact location of rockfalls on static elements (Mavrouli & Corominas, 2010), their exposure is directly provided by the reach probability. In contrast, the probability to impact a moving object must be adjusted by the probability to which the latter is in the path of the rockfall (spatial probability) at the time of its occurrence (temporal probability; Lambert, 2011; Corominas et al., 2014; Budetta et al., 2016). Also, the exposure component for moving elements must integrate the characteristics of traffic intensity.

3.3 | Earthquake-induced rockfalls

3.3.1 | Magnitude of seismic activity in Uspallata valley

Earthquakes can be considered as the main drivers for rockfall activity at our study area. In that respect, an in-depth knowledge and understanding of the local seismic hazard is necessary for evaluating seismically induced rockfall risk. The seismicity in Central Chile is controlled by the subduction of the Nazca plate under the south American plate, which generates interface and intraslab earthquakes with a wide range of magnitudes. The PGA seismic hazard curve was derived from a probabilistic seismic hazard analysis (PSHA; Candia et al., 2019), which is a customary tool in research and engineering seismology to characterize the ground shaking intensity to which a specific site may be subjected within a period of time by taking into account all possible scenarios and their respective rate. For a region consisting of N_s seismic sources, the annual rate of exceedance Λ of a given PGA value (x) can be expressed as (Candia et al., 2019):

$$\Lambda(pga > x) = \sum_{h=1}^{N_s} N^h(M_{min}) \int_{m=M_{min}}^{M^h_{max}} \int_{r=0}^{R_{max}} \Pr(pga > x \mid m, r)\, f^h_M(m)\, f^h_R(r, m)\, dr dm\,, \quad (8)$$

where the term $N^h(M_{min})$ is the activity rate of the hth seismic source, defined as the average number of earthquakes per year with magnitude greater than or equal to a magnitude threshold M_{min}. $f^h_M(m)$ is the probability density function for the earthquake magnitude distribution of the hth source, and $f^h_R(r, m)$ the probability density function of the site-to-source distance, which is a function of the site location, the source geometry, and the rupture area model adopted. Finally, the probability term $\Pr(pga > x \mid m, r)$ is the conditional probability that pga exceeds x given an earthquake of magnitude m at a distance r from the source and is obtained from a ground motion model (GMM; Candia et al., 2019).

The seismic hazard at the site of interest (2.35 hm^2 cliff section located above the 200-m-long transect) was thus expressed as the mean annual rate of exceedance of a ground motion intensity parameter (the PGA), using a probabilistic framework that accounts for uncertainties in earthquake size, earthquake location, and rupture area, as well as the scientific uncertainty from alternative models of the problem. It is also assumed that the occurrence of an earthquake of a certain magnitude is independent of the time since the last earthquake, so that the earthquake recurrence follows a Poisson process (Table 1). For all the hazard computations, we implemented the software Seismic Hazard (Candia et al., 2019) using the slab geometry as proposed by Hayes et al. (2012), and the seismic sources by Poulos et al. (2019).

3.3.2 | Critical ground acceleration allowing block motion

Knowing the seismic hazard curve, the minimal ground acceleration required to initiate slope failure hereafter yield acceleration, A_c (in g), must be assigned to each cell in the grid. For this purpose, we used the yield acceleration model developed by Wilson and Keefer (1985) (Table A). In greater detail, groundwater condition is divided into either dry condition (groundwater below the sliding surface) or wet condition (groundwater level at or above the sliding surface). Geological properties are identified for three sets of lithologies: strongly cemented rocks (crystalline rock and well-cemented sandstone), weakly cemented rocks (sandy soil and poorly cemented sandstone), and argillaceous rocks (shales, clayey soil, existing landslides, poorly compacted fills). Finally, by assuming that a slope failure within a rocky wall induces the detachment of one individual rock mass, the annual frequency of seismically induced rockfall is obtained by the intersection of A_c value with the seismic hazard curve.

4 | APPLICATION

4.1 | Rockfall release areas

Identification of potential rockfall release areas is a challenging task, especially in this study. Difficulties stem from (i) the large extent of the site and (ii) the limited resolution (30 ×30 m) of the ASTER (GDEM.V2) DEM at hand, which precludes from a precise detection of rockfall sources. Consequently, DEM-based geomorphometric approaches usually employed for the identification of potential release areas (Loye et al., 2009; Michoud et al., 2012) were not found suitable at our study site. Potential rockfall release areas were rather defined from the large-scale geomorphological

map supplied by the Instituto Geográfico Militar de Chile on which vertical rock-covered surfaces are well identified. This sketch was assessed by extensive field observations. Indeed, several subvertical sources, easily detectable given the numerous open cracks and partially detached rock blocks on cliff, as well as the high number of blocks accumulated downslope, are not included in the geomorphic maps. The latter were thus added to our susceptibility map, thereafter integrated into a Geographical Information System (GIS) and converted in a raster layer of 10 m resolution, yielding 191,780 starting cells. These sources were evaluated to correspond to a total surface of 2714 hm^2.

4.2 | Temporal occurrence of rockfall events

4.2.1 | Total rockfall frequency

In addition to susceptibility, the temporal probability of failure must be assessed to define the probability of the occurrence of a rockfall event (Ferrari et al., 2016). For this purpose, 104 blocks with volumes ranging from 0.5 m^3 to 19.5 m^3 were inventoried through detailed field observations along a 200-m-long transect located downslope of switchbacks on way up to Portillo (Figure 2B). This transect was chosen for (1) its accessibility and proximity to the cliff, (2) its representativeness (diversity of block volumes), and (3) the low probability of block removal due to human or snow avalanche activities. The rockfall sources that potentially released the 104 blocks were evaluated to correspond to a total surface (R_s) of 2.35 hm^2. Unfortunately, the absence of historical rockfall inventory results in uncertainties relating to the temporal window for the sampled blocks. In that respect, we assumed that the reference period for the computation of rockfall frequency does not exceed 10,000 years (T_w, end of the last glacial period; Table 1). Considering that rockfall starting points are homogeneously distributed on the rocky cliff, the rockfall frequency per year and per hm^2 was thus estimated at 0.0044 events/year/hm^2. By taking into consideration the whole cliff surface (2714 hm^2; Section 4.1), the frequency of rockfall events, λ, was found equal to 12 events/year.

4.2.2 | Rockfall frequency for seismic and meteorological triggers

On the basis of the DEM (30 × 30 m), the mean slope angle at the site located above the 200-m-long transect (2.35 hm^2 cliff section) was evaluated at 49°. Assuming strongly cemented rocks lithology and dry condition in Uspallata, the landslide susceptibility for the site of interest was evaluated as category VI (Table A). In that respect, the yield acceleration A_c equals 0.25 g (Table B). Based on the seismic hazard assessment for the 2.35 hm^2 cliff section, the annual frequency of seismically induced rockfall was therefore estimated at 0.0061 events/year (Figure 4).

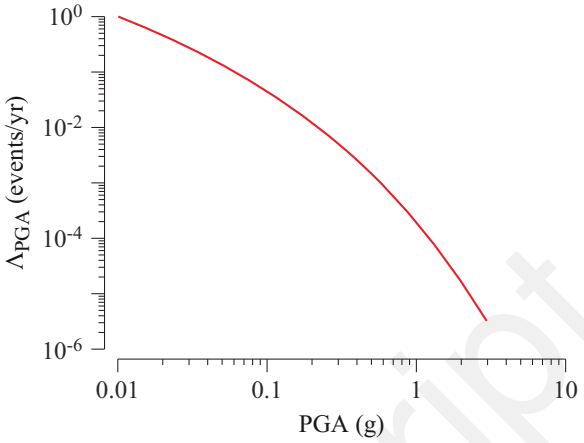

FIGURE 4 Seismic hazard curve providing the annual rate of exceedance as function of peak ground acceleration (PGA) in the Uspallata valley.

Based on the assumption that a slope failure within the 2.35 hm^2 rocky wall induces the detachment of one individual rock mass (Table 1), 61 rockfall events (out of the 104 blocks inventoried along the 200-m-long transect) should thus have been released from this specific cliff section in the last 10,000 years due to seismic activity. In that respect, the annual frequency of rockfall initiation from earthquake activity equal 0.0026 events/year/hm^2 (61 events/ 10,000 years × 2.35 hm^2). Considering the surface of the whole cliff over the study area (2714 hm^2; Section 4.1), the frequency of seismically induced rockfall events is therefore 7 events/year (λ_{T_S}, 59% of λ). Finally, it is known that seismicity is not the only trigger of rockfall activity in Uspallata (Moreiras, 2006). Under the simple assumption that all events that were not triggered by earthquakes are due to meteorological conditions (in a broad sense: freeze–thaw cycles, intense precipitation, etc.), the remaining 5 events/year (λ_{T_M}, 41% of λ) were considered as meteorologically triggered events (0.0018 events/year/hm^2).

However alternative GMMs can be used to assess the seismic hazard curve at the site of interest. To assess the sensitivity to the choice of the GMM, our approach has thus also been tested for five different GMMs from existing literature (Table C). Regardless the model, λ_{T_S} varies from 5.06 events/year (42% of λ) to 9.29 events/year (77% of λ). On average, these values remain relatively close to the initial one (7.148 events/year).

4.3 | Magnitude of the events

4.3.1 | Total rockfall volume distribution

The probability distribution of rockfall volumes regardless triggering mechanisms was obtained by fitting the GPD (Coles, 2001) using the maximum likelihood procedure on inventoried rockfall events (Section 4.2.1). The threshold u = 0.5 m^3 was used here as we consider it as the minimum

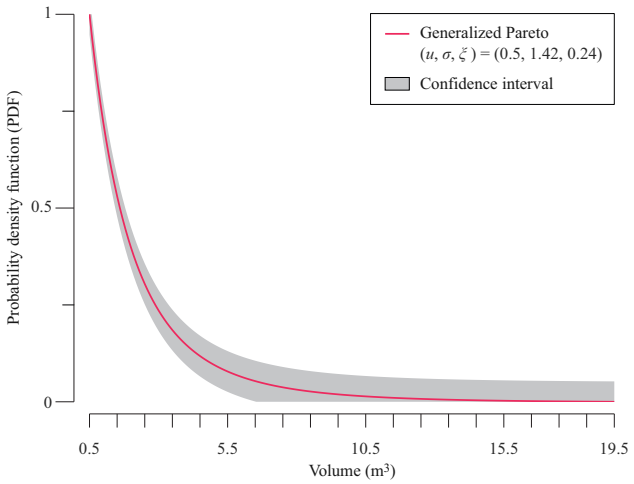

FIGURE 5 Probability density function of rockfall volumes (red line) obtained by an asymptotic model of the generalized Pareto distribution (GPD) family and related to rock volumes inventoried along a 200-m-long transect. The shaded area illustrates the model 95% confidence interval.

volume that can produce significant damage regardless the nature of exposed elements. This resulted in maximum likelihood estimates σ and ξ equal to 1.42 and 0.24, respectively (Figure 5). Since an upper bound for released volumes was set (19.5 m^3), frequencies were normalized by $1 - \int_{19.5}^{\infty} GPD(\sigma, \xi)$ to obtain a probability density function with a total probability of one. Based on Equation (6), the rockfall probabilities in the discretized volume classes 0.5–1.5 m^3 and 18.5–19.5 m^3 are to 0.4789 and 0.0005, respectively.

4.3.2 | Rockfall volume distribution for seismic and meteorological triggers

In rockfall risk studies, volume distributions are always assumed to be independent of the triggering factors. Furthermore, to our knowledge, no study focused on the variation of rockfall volume distribution as function of their drivers. In practice, we are aware that such an approach is challenging due to many epistemic uncertainties that refer, for example, to the lack of data. In this study, we nevertheless accounted for a possible correlation between rockfall volume distribution and triggering mechanisms by introducing different volume distribution scenarios as inputs for risk assessment. The objective is to evaluate the respective proportions of each triggering factor in the total risk, and how these proportions are sensitive to assumptions regarding input distribution scenarios.

By assuming that earthquake and meteorological events are the main drivers of rockfall activity at Uspallata, we introduced three rockfall volume distribution scenarios (D0, D1, and D2), each of them representing a different weighting among volume classes between seismic (T_S) and meteorological (T_M) drivers. In the first scenario (D0), we assumed the same probability distribution of volumes whatever the triggering factor. The respective weight in each volume class was assigned following the probability distribution obtained for the GPD model (Section 4.3.1; Figure 2). For rockfall volume distribution scenarios D1 and D2, we hypothesized that seismic activity was the preferential trigger for large rockfall. This assumption arises from the large rock blocks observed after the 2015 M_w 8.3 Illapel, Chile earthquake (Candia et al., 2016; Table 1). Hence, in scenario D1, probabilities of 0.6 and 0.3 were set to meteorological-induced rockfall events in volume classes 0.5–1.5 m^3 and 1.5–2.5 m^3, respectively, so that seismic activity is the main trigger of rockfall events > 2.5 m^3. Further, as an extreme case, in scenario D2, meteorological triggers were only assumed in volume classes ranging from 0.5 m^3 to 1.5 m^3 (Table 1). In that respect, earthquake activity was considered as the sole triggering factor of rockfall in volume classes exceeding 1.5 m^3. Hence, these scenarios cover the whole range of possible partitioning between meteorological and earthquake-induced triggers, between even weighs of both triggers in all volume classes to the most extreme weights of large volumes in earthquake triggers. A detailed summary is provided in Table 2 and the calculation of the respective weight of each triggering factor among volume classes is addressed in Equation (D).

4.4 | Rockfall propagation and damage

The LULC map integrated into Rockyfor3D was derived from field observations. Given the sparse vegetation and a coarse soil composed with small rock fragments, the vast majority of the study area is described by a medium compact soil ($r_n = 0.33$). The roughness component is evaluated for three variables, representing the obstacle height encountered on 10% (Rg10), 20% (Rg20), and 70% (Rg70) of the surface, respectively. The landforms resulting from fluvial deposits along the main rivers of the site (Figure 2) are given roughness values of 0.05 m (Rg10), 0.05 m (Rg20), and 0.03 m (Rg70). In transit allotments (from cliff to river), bare terrains are mainly flat. Roughness values of 0.05 m, 0.05 m, and 0.00 m (Rg70) are thus assigned to Rg10, Rg20, and Rg70, respectively.

On the basis of the 30-m-resolution DEM (ASTER GDEM.V2), 1900 rockfalls with volumes randomly and uniformly extracted among 19 equal volume classes in the range 0.5 m^3 and 19.5 m^3 were simulated at each of the 191,780 source cells, yielding 364,382,000 simulations (19,178,000 simulated blocks in each volume class). Despite larger block volumes could be observed in Uspallata, our analysis was limited to 19.5 m^3 in order to comply with Rockyfor3D's validity range.

In Uspallata, exposed elements involve buildings, hydroelectric power plants, and vehicles (cars, pickups, buses, trucks, and trains) circulating on transport lifelines (i.e., road No. 60 and Transandino open path). To provide a detailed analysis of rockfall risk for vehicles along transportation corridors, the latter were divided in 10-m sections. Also, buildings were considered on an individual basis

TABLE 2 Probability of rockfall volume among 19 equal volume classes v_{Cl} for three distribution scenarios D0, D1, D2. Each scenario represents different weighting among volume classes between seismic (T_S) and meteorological (T_M) triggered rockfall (Equation D). The first scenario was designed assuming the same probability distribution of volumes whatever the triggering factor. The respective weighting among volume classes was assigned based on the probability distribution obtained for the GPD model (Section 4.3.1; Figure 2). Scenarios D1 and D2 were both developed assuming that seismic events were the best triggering potential for largest block volumes. In scenario D1, seismicity was considered as the main trigger of rockfalls exceeding 2.5 m^3. In scenario D2, a meteorological-rockfall coupling was only considered in the volume class ranging from 0.5 m^3 to 1.5 m^3 (probability of 1). Probabilities were assigned respecting a total probability of one.

	Dist. scenario D0		**Dist. scenario D1**		**Dist. scenario D2**	
	T_S	T_M	T_S	T_M	T_S	T_M
v_{Cl_1} (0.5–1.5 m^3)	0.4789	0.4789	0.3944	0.6000	0.1151	1.0000
v_{Cl_2} (1.5–2.5 m^3)	0.2246	0.2246	0.1720	0.3000	0.3815	0.0000
v_{Cl_3} (2.5–3.5 m^3)	0.1163	0.1163	0.1627	0.0500	0.1976	0.0000
v_{Cl_4} (3.5–4.5 m^3)	0.0650	0.0650	0.1034	0.0100	0.1104	0.0000
v_{Cl_5} (4.5–5.5 m^3)	0.0386	0.0386	0.0589	0.0095	0.0655	0.0000
v_{Cl_6} (5.5–6.5 m^3)	0.0240	0.0240	0.0352	0.0080	0.0408	0.0000
v_{Cl_7} (6.5–7.5 m^3)	0.0156	0.0156	0.0212	0.0075	0.0265	0.0000
v_{Cl_8} (7.5–8.5 m^3)	0.0105	0.0105	0.0146	0.0045	0.0178	0.0000
v_{Cl_9} (8.5–9.5 m^3)	0.0072	0.0072	0.0107	0.0022	0.0123	0.0000
$v_{Cl_{10}}$ (9.5–10.5 m^3)	0.0051	0.0051	0.0075	0.0017	0.0087	0.0000
$v_{Cl_{11}}$ (10.5–11.5 m^3)	0.0037	0.0037	0.0053	0.0014	0.0063	0.0000
$v_{Cl_{12}}$ (11.5–12.5 m^3)	0.0027	0.0027	0.0040	0.0010	0.0047	0.0000
$v_{Cl_{13}}$ (12.5–13.5 m^3)	0.0021	0.0021	0.0029	0.0009	0.0035	0.0000
$v_{Cl_{14}}$ (13.5–14.5 m^3)	0.0016	0.0016	0.0021	0.0008	0.0027	0.0000
$v_{Cl_{15}}$ (14.5–15.5 m^3)	0.0012	0.0012	0.0016	0.0007	0.0021	0.0000
$v_{Cl_{16}}$ (15.5–16.5 m^3)	0.0010	0.0010	0.0012	0.0006	0.0016	0.0000
$v_{Cl_{17}}$ (16.5–17.5 m^3)	0.0008	0.0008	0.0009	0.0005	0.0013	0.0000
$v_{Cl_{18}}$ (17.5–18.5 m^3)	0.0006	0.0006	0.0007	0.0004	0.0010	0.0000
$v_{Cl_{19}}$ (18.5–19.5 m^3)	0.0005	0.0005	0.0006	0.0003	0.0008	0.0000

and introduced in Rockyfor3D as obstacles with infinite height and resistance. Simulations reaching buildings were therefore automatically stopped, in contrast with road/rail sections where we assumed that vehicles are not resistant for stopping the falling block in its propagation (Table 1).

For each simulation reaching a building or a linear section, the volume of the block and its kinetic energy (in kJ), as well as the simulation, impacted object and starting cell IDs were therefore recorded in a database. The position of elements at risk z combined with rockfall trajectories allow to quantify reach probabilities. Additionally, impact energies resulting from the Rockyfor3D model were derived in terms of damages. For structural elements, damages were quantified from the empirical vulnerability function developed by Agliardi et al. (2009) (Equation 7). For vehicle, given the numerous and severe rockfall damages observed on the field on road and rail tracks (impact marks, irregular depressions, severely impacted retaining walls) in Uspallata valley, the damaging value d regardless rockfall energy was set to a value of 1.

Finally, in order to quantify the potential number of fatalities per year resulting from rockfall activity in the Uspallata valley, the QRA performed in this study has been extended to people. To this end, the local population (1395 persons according to the Centro Nacional de Investigación para la Gestión Integrada de Desastres Naturales CIGIDEN) was homogeneously distributed over the dwelling houses mapped in the studied area (occupancy rate of 0.008 person/m^2) and the physical vulnerability for a person within an impacted building was set to 0.9 (Corominas & Mavrouli, 2013). For any vehicle traveling on road No. 60, we assumed that a person inside a vehicle impacted by a rockfall event has no chance of survival after the crash.

4.5 | Exposure and value of elements at risk

The exposure factor was evaluated for each road and rail section (10-m length) by distinguishing cars, pickups, buses, trucks, and trains. For this purpose, we assumed that (i) the traffic is uniformly distributed in space and time (i.e., no slow down of traffic or jams; Table 1) and (ii) damages result from a direct impact of a falling block. Also, the exposure component for vehicles must integrate the characteristics of traffic intensity, such as their frequency and their mean velocity. Vehicle lengths and speeds were determined from field observations and annual averages of daily traffic were provided by ANID-CIGIDEN (Centro Nacional de Investigación para la Gestión Integrada de Desastres Naturales) for each type of

TABLE 3 Parameters for exposure calculations based on each type of vehicle. Vehicle lengths and speeds have been determined from field observations. Annual averages of daily traffic have been provided by ANID/CIGIDEN (Centro Nacional de Investigación para la Gestión Integrada de Desastres Naturales) for each type of vehicle. Given the lack of data on mining operation trains, corresponding values are estimates developed for this specific study.

z	l (m)	v (m/s)	τ (daily traffic)
Car	5	25	600
Pickup	6	25	235
Bus	12	20	75
Truck	12	20	1,073
Train	100	14	1

vehicle. Given the lack of data on mining operation trains, corresponding values are estimates developed for this specific study. The length, speed, and daily traffic of vehicles are summarized in Table 3. Contrary to vehicles and trains, buildings are static and consequently exposure factor is inexorably 1. For people, the exposure value is set to 0.5 by considering an occupation of the house 12 hours per day.

The value Z_w was primarily defined as the cost of the element at risk z, expressing the risk in monetary terms ($/year). The choice of this unit stems (1) from the necessity to harmonize results and to assess the amount of money necessary for disaster recovery (Melching & Pilon, 1999) and (2) from our motivation to increase decision makers' awareness for rockfall risk mitigation, with potential inclusion of countermeasures in cost–benefit considerations. For buildings, cost values were approximated by multiplying the floor area (in m^2) of the structure by the average price (in US dollars) per m^2 of a typical building in the province of Los Andes. Based on local current land prices, this value corresponded to 1440$/$m^2$. A highest floor price of 2300 $/$m^2$ was given to hydroelectric plants. Regarding vehicles, Z_w was given by their average buying price. Values of $9000, $11,000, $221,000, $166,000, and $1,200,000 were given to car, pickup, bus, truck, and train, respectively. Eventually, risk to people was quantified as a lethality rate, for which Z_w is an individual life.

4.6 | Risk estimates

4.6.1 | Total rockfall risk

Risk analysis was performed numerically on a case-by-case basis by distinguishing each element at risk z identified in the system w. The risk value (expressed as an expected monetary loss per year or as a lethality rate) specific to each element z was approximated by discrete sums on all volume classes v_{Cl}. The risk for the element z was therefore given by:

$$\overline{\mathrm{R}}_z = Z_w \sum_{i=1}^{l} q(z_w \mid v_{Cl_i}) \times f(v_{Cl_i}) \times p_z(v_{Cl_i}) \times \overline{d}_z(v_{Cl_i}). \quad (9)$$

Based on the rockfall volume distribution (Equation 6), the rockfall frequency per volume class was assessed by multiplying the temporal occurrence probability, λ, by the probability of rockfalls to occur in the volume class, $\Pr\{\mathrm{V} \in v_{Cl_i}\}$, as:

$$f(v_{Cl_i}) = \lambda \times \Pr\{\mathrm{V} \in v_{Cl_i}\}. \quad (10)$$

Additionally, the reach probability at each z for block volumes in v_{Cl_i} was determined as the ratio of rockfall trajectories passing at position z with volumes belonging to v_{Cl_i}, $\mathrm{Sim}_z(v_{Cl_i})$, and the total number of simulated blocks in each volume class, $\mathrm{Sim}(v_{Cl_i})$:

$$p_z(v_{Cl_i}) = \frac{\mathrm{Sim}_z(v_{Cl_i})}{\mathrm{Sim}(v_{Cl_i})}. \quad (11)$$

Then, for each volume class v_{Cl_i}, the mean damage $\overline{d}_z(v_{Cl_i})$ was approximated by a Monte Carlo simulation as:

$$\overline{d}_z(v_{Cl_i}) = \frac{1}{n} \sum_{k=1}^{n} d(z, E_k), \quad (12)$$

where E_k, $k \in [1, n]$, is the local distribution of rockfall energies for blocks belonging to the volume class v_{Cl_i} conditional to reach.

For moving elements, the exposure factor $q_z(v_{Cl_i})$ for blocks belonging to the volume class v_{Cl_i} was calculated by considering the daily traffic density as:

$$q(z_w \mid v_{Cl_i}) = \mathrm{Sp}_z(v_{Cl_i}) \times \mathrm{Tp}_z \times \tau_z, \quad (13)$$

where $\mathrm{Sp}_z(v_{Cl_i})$ and Tp_z correspond to the spatial and temporal probability of a moving vehicle z to encounter a block belonging to the volume class v_{Cl_i}, respectively, and τ_z to the annual average daily traffic of vehicles z.

Following Michoud et al. (2012), the spatial probability of a moving vehicle z to encounter a block belonging to the volume class v_{Cl_i} in a predefined section was given by:

$$\mathrm{Sp}_z(v_{Cl_i}) = \begin{cases} \left[\varnothing(v_{Cl_i}) + l(z)\right] \times \left[1/L\right] & \text{if} \quad \varnothing(v_{Cl_i}) + l(z) < L \\ 1 & \text{otherwise} \end{cases}, \quad (14)$$

where $l(z)$ is the average length of the moving vehicle and L the length of the transport lifeline section. $\varnothing(v_{Cl_i})$ represents the mean diameter of a block volume belonging to the volume class v_{Cl_i} and is derived from spherical block shapes. Lengths are expressed in meters.

Furthermore, by assuming that the exposure time of a vehicle to rockfalls corresponds to the elapsed time between its entrance in the transport lifeline section and its total exit, the temporal probability of a moving vehicle to encounter a block belonging to the volume class v_{Cl_i} every day in a year was expressed as:

$$\mathrm{Tp}_z = \frac{l(z) + L}{v_z} \times \frac{1}{24 \times 60 \times 60}, \quad (15)$$

where v_z is the mean velocity of the vehicle (in m/s).

Finally, the total risk for the system w is the sum of individual risks for all elements of the system w (Eckert et al., 2012), that is,

$$\overline{\mathrm{R}}_w = \sum_{z \in w} \overline{\mathrm{R}}_z \,. \tag{16}$$

4.6.2 | Risk as function of rockfall triggers

Seismically induced rockfall risk is evaluated numerically as:

$$\overline{\mathrm{R}}_w(\mathrm{T_S}) = \sum_{z \in w} Z_w \times \sum_{i=1}^{l} q(z_w |\, v_{Cl_i}) \times \lambda_{\mathrm{T_S}} \times \Pr\{\mathrm{V} \in v_{Cl_i} |\, \mathrm{T_S}\} \times p_z(v_{Cl_i}) \times \overline{d}_z(v_{Cl_i}) \,. \tag{17}$$

Given the assumption that seismic activity and meteorological conditions are the sole rockfall triggering factors, meteorological-induced rockfall risk is:

$$\overline{\mathrm{R}}_w(\mathrm{T_M}) = \overline{\mathrm{R}}_w - \overline{\mathrm{R}}_w(\mathrm{T_S}). \tag{18}$$

Finally, the respective weight (Wt) of each triggering factor in total risk is thus given by:

$$\mathrm{Wt}(\mathrm{T_S}) = \overline{\mathrm{R}}_w(\mathrm{T_S})/\overline{\mathrm{R}}_w. \tag{19}$$

$$\mathrm{Wt}(\mathrm{T_M}) = \overline{\mathrm{R}}_w(\mathrm{T_M})/\overline{\mathrm{R}}_w. \tag{20}$$

4.6.3 | Sensitivity analysis

A comprehensive rockfall risk assessment is difficult due to many epistemic and aleatory uncertainties. The challenge also stems from the models themselves and the various assumptions they include. A sensitivity analysis was therefore conducted to identify the components most susceptible to influence the risk evaluation and assess the overall robustness of the estimates provided. This analysis involved rerunning the QRA calculation, using iteratively new input variables/parameters, and leaving all other assumptions unchanged. To this aim, in addition to the already mentioned sensitivity analysis to the GMM, we first identified the components that are considered to be prone to uncertainty, that is, the value of elements at risk Z_w, the average length of moving vehicle $l(z)$ (Equation 14), the mean velocity of vehicle v_z (Equation 15), the annual average daily traffic of vehicles τ_z (Equation 13), the source surface R_s (Section 4.2.1), the reference period T_w (Section 4.2.1), the number of rockfall trajectories passing at z with volumes belonging to v_{Cl_i}, $\mathrm{Sim}_z(v_{Cl_i})$ (Equation 11), the mean damage $\overline{d}_z(v_{Cl_i})$ (Equation 12), and the GPD model (σ and ξ). Uncertainties related to rockfall triggers (rockfall frequencies for seismic and meteorological triggers) were not considered as they do not influence total risk estimates. New input variables were then defined by increasing or decreasing the initial value by a percentage X% representing a potential percentage of uncertainty. Specific error estimates were used for the GPD model (95% confidence interval; Figure 5). The new input values were thereafter implemented in the QRA procedure so that the effect of isolated changes in inputs on total rockfall risk can be measured.

5 | RESULTS

5.1 | Probability and energy of rockfall impacts

The total surface of the potential release areas was evaluated at 2,714 hm^2 and consequently, following Equation (10), the frequency of rockfall in the volume classes 0.5–1.5 m^3 and 18.5–19.5 m^3 were estimated at 5.76 and 0.006 events/year, respectively. These results were refined by considering specifically seismic and meteorological triggering factors under the rockfall volume distributions D0, D1, and D2 (Figure 6; Table 2). Assuming the same volume distribution (GPD distribution) regardless of the triggering factor (volume distribution D0), the seismically induced rockfall frequency in the volume classes 0.5–1.5 m^3 and 18.5–19.5 m^3 were estimated at 3.392 and 0.003 events/year, respectively. Consequently, these values equal 2.368 and 0.002 events/year for blocks triggered by meteorological events, respectively (Figure 6A). Based on the rockfall volume distribution D1, the seismically induced rockfall frequency of rockfalls in the volume classes 0.5–1.5 m^3 and 18.5–19.5 m^3 were estimated at 2.793 and 0.004 events/year, respectively. In contrast, meteorological factors release 2.967 and 0.0015 events per year in the volume classes 0.5–1.5 m^3 and 18.5–19.5 m^3 (Figure 6B). Finally, the seismically induced rockfall frequency with volume distribution D2 were evaluated at 0.815 and 0.006 events/year in the volume classes 0.5–1.5 m^3 and 18.5–19.5 m^3, respectively. These values therefore equal 4.945 and 0 events/year for blocks triggered by meteorological events, respectively (Figure 6C).

Regardless of the volume class, 180,315,768 (50%) out of the 364,382,000 rockfall simulations performed reached the different identified units (buildings, power plants, road and rail network), resulting in a total of 372,569,238 rockfall impacts (rockfalls are not stopped when reaching transport sections, potentially threatening stakes located further downslope). In greater details, 4,614,782 (1% of the total number of impacts); 198,793 (< 1%); 356,274,877 (96%); and 11,480,786 (3%) impacts were recorded on 169 buildings, 14 hydroelectric power plants, 3928 10-m road sections, and 1020 10-m railway sections, respectively. In other words, the probability to be reached by a rockfall event is strictly above 0 for 25%, 74%, 56%, and 37% of the buildings, hydroelectric power plants, road network cells, and train network cells within the study area, respectively.

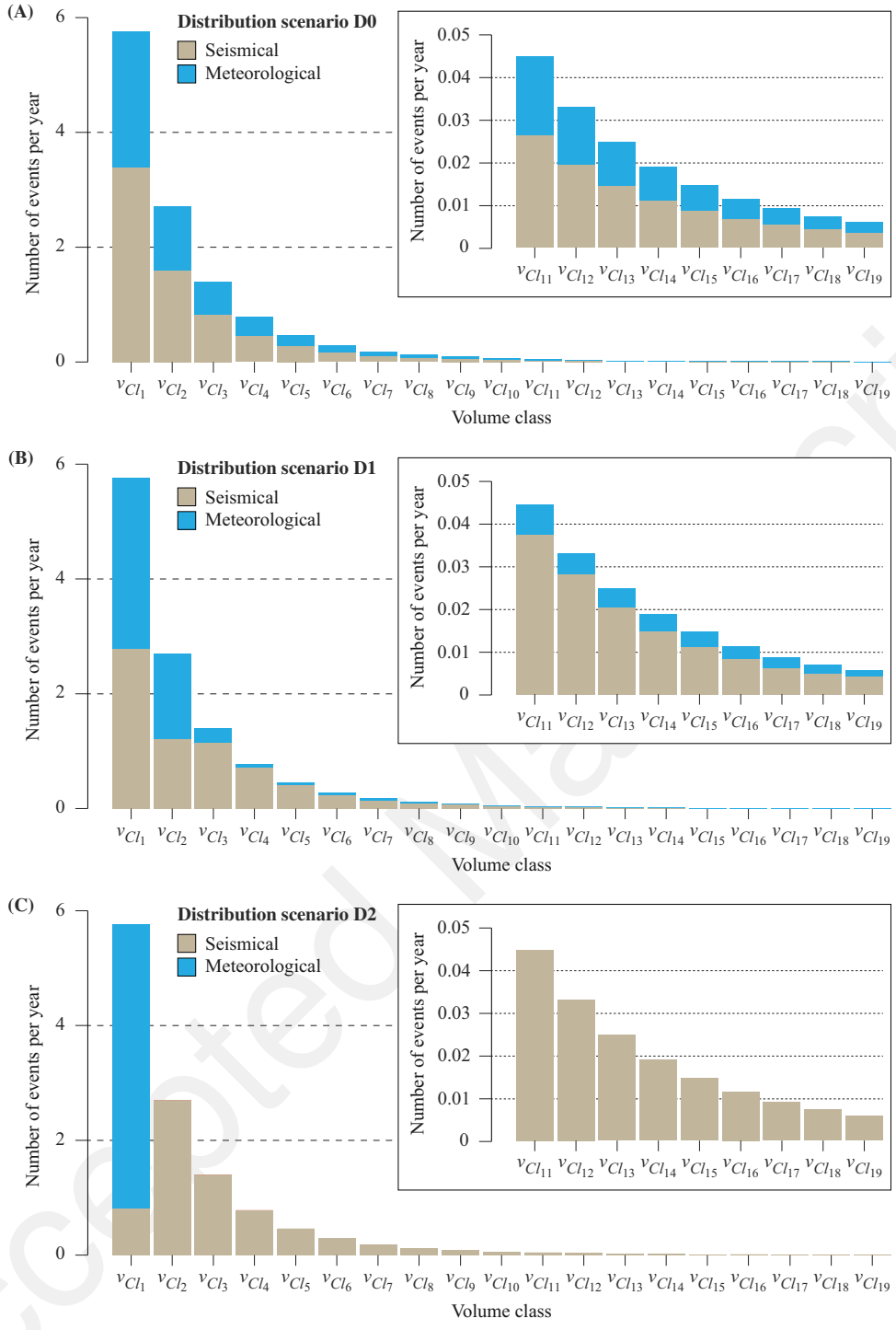

FIGURE 6 Volume–frequency distributions (number of events per year) in the Uspallata valley obtained for the three distribution scenarios D0 (A), D1 (B), and D2 (C) representing different weighting among volume classes between seismic and meteorological triggered rockfall (Table 2).

With regard to the intensity of rockfall simulations, 96% of the blocks stopped by impacting buildings are characterized by kinetic energies > 1000 kJ. Among these values, a maximum energy of 76,410 kJ has been recorded for a block volume of 19.4 m^3. The energies of rockfall impacts at the level of each building and hydroelectric power plant were converted into a damage level based on the empirical vulnerability function developed by Agliardi et al. (2009). Not surprisingly, these values were equal to 1 for the vast majority of the impact energies, leading to the total destruction of the considered building.

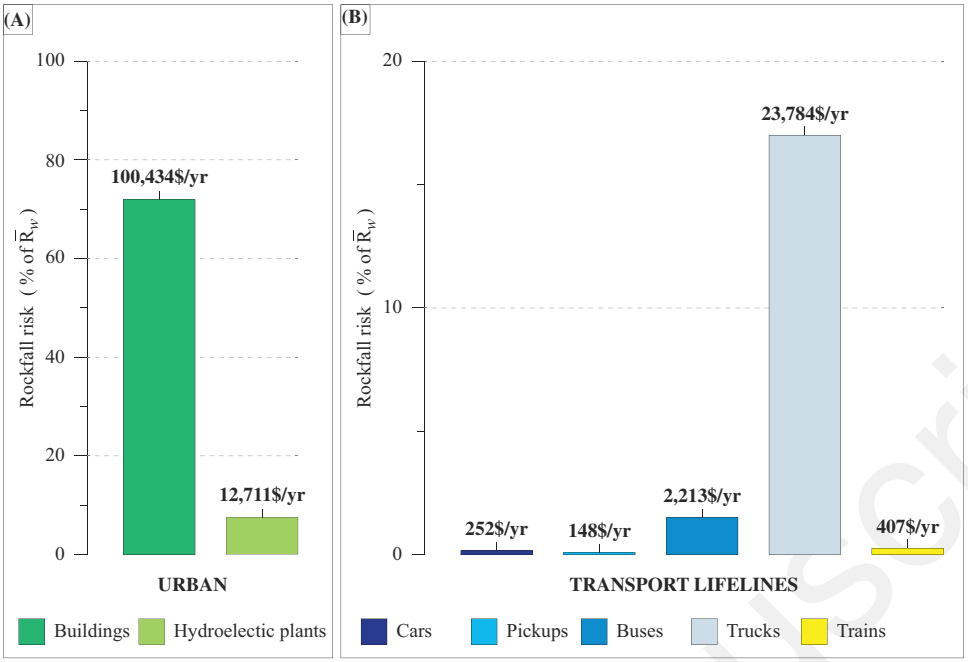

FIGURE 7 Rockfall risk (in $/year and % of the total risk value $\overline{R}_w$) for the urban area (A) and vehicles circulating on transport lifelines (B). In total, the rockfall risk $\overline{R}_w$ reaches 139,951 $/year.

5.2 | Exposure of elements at risk

The spatial probability for cars and pickups in linear sections of 10 m to encounter a block within the volume class 0.5–1.5 m^3 is equal to 0.624 and 0.724, respectively. These values increase to 0.831 (cars) and 0.931 (pickups) for blocks within the 18.5- to 19.5-m^3 range. Regarding buses, trucks, and trains, the spatial probability is 1 regardless of the volume class ($l > L$). Similarly, based on Equation (15), the temporal probability to encounter a block in a 10-m section is 6.95^{-6} (car), 7.41^{-6} (pickup), 1.31^{-6} (bus and truck), and 9.17^{-6} (train).

Based on the annual average daily traffic and both the temporal and spatial probabilities, exposures of cars and pickups (in the 10-m-length sections) to rockfalls in the volume class 0.5–1.5 m^3 are equal to 0.0026 and 0.0013, respectively. These values are equal to 0.0035 (cars) and 0.0016 (pickups) for blocks ranging between 18.5 and 19.5 m^3. Regardless the volume class, exposure of buses, trucks, and trains are 0.0010, 0.0140, and 9^{-5}, respectively.

5.3 | Rockfall risk

5.3.1 | Total risk to property

The risk associated to rockfall activity has been determined for block volumes in the range 0.5–19.5 m^3. Following Equation (16), the total risk $\overline{R}_w$ reaches 139,951 $/year. In greater detail, 81% of $\overline{R}_w$ results from static elements (Figure 7). Buildings account for 72% of $\overline{R}_w$ (100,434 $/year), and hydroelectric plants for 9% of $\overline{R}_w$ (12,711.5 $/year). The remaining 19% of the total risk is associated to transport lifelines (Figure 7). The risk associated with the road No. 60, regardless of the vehicles, is 26,398$/year (18.8% of $\overline{R}_w$). Cars (252 $/year) and pickups (148 $/year) represent 0.3% of $\overline{R}_w$ (400 $/year), against 1.5% for traffic of buses (2213 $/year). For truck traffic, the risk (17% of $\overline{R}_w$; 23,784 $/year) is significantly higher. In contrast, the risk for train traffic is limited (< 1% of $\overline{R}_w$; 407 $/year; Figure 7).

Spatially, among the 170 out of the 682 buildings impacted by rockfall simulations, 49 have an annual rockfall risk > 100 $/year (Figure 8A). A maximal value of 25,034$/year (18% of $\overline{R}_w$) was recorded on the toll (Figure 2A). On the contrary, no impact was recorded on the ski resort of Portillo (Figure 2A), obviously resulting in a rockfall risk of 0 $/year. Similarly, the rockfall risk is > 100 $/year for 16% of the hydroelectric power plants and a maximum value of 11,521 (8% of $\overline{R}_w$) was recorded for the hydroelectric power plant located between the municipality of Rio Blanco and the toll (Figure 2A).

Finally, the risk associated to rockfall activity has been detailed for each 10-m road and rail sections. Regardless the vehicle type, the risk per section exceeds 100 $/year over about 140 m of the road No. 60 (about 0.2% of the road). Unsurprisingly, the latter sections are located between the toll and the transect chosen for field analysis (Figure 9A). In total, the potential loss resulting from these high-risk sections amounts 1993 $/year (1.4% of $\overline{R}_w$) of which about 90% (1795 $/year) result from truck traffic. Finally, the risk resulting from train traffic is very low for a large majority of the sections.

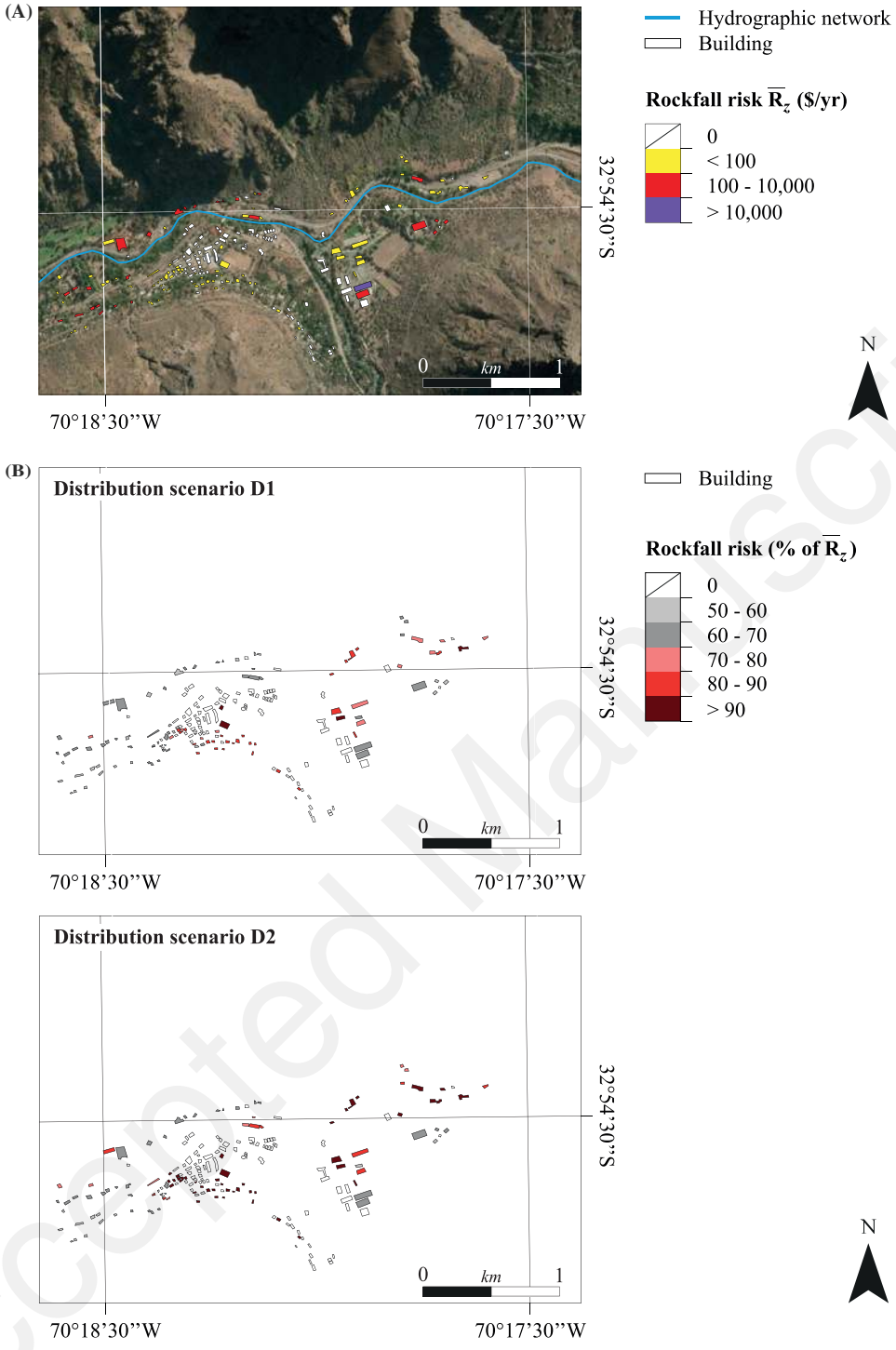

FIGURE 8 (A) Rockfall risk (i.e., annual expected cost in dollars) computed for single buildings. Given the size of the site, the map focuses on the municipality of Rio Blanco (white square A on Figure 2A). The rockfall risk associated to this specific area is equal to 22,259 $/year. (B) Rockfall risk resulting from seismic events (% of the risk value $\overline{R}_z$) for rockfall volume distribution scenarios D1 and D2. The rockfall risk resulting from the volume distribution scenario D0 corresponds to 59% of $\overline{R}_z$ regardless the element at risk.

5.3.2 | Total risk to people

The QRA performed in this study has been extended to people in order to assess the potential number of fatalities per year resulting from rockfall activity in the Uspallata valley. Overall, the risk to people within houses reaches 0.07 fatalities/year (one fatality every 14 years). Interestingly, 28% of the fatalities (0.02 fatalities/year, one fatality every 50 years) result from a unique house located in the municipality of Rio Blanco. More generally, the annual casualty

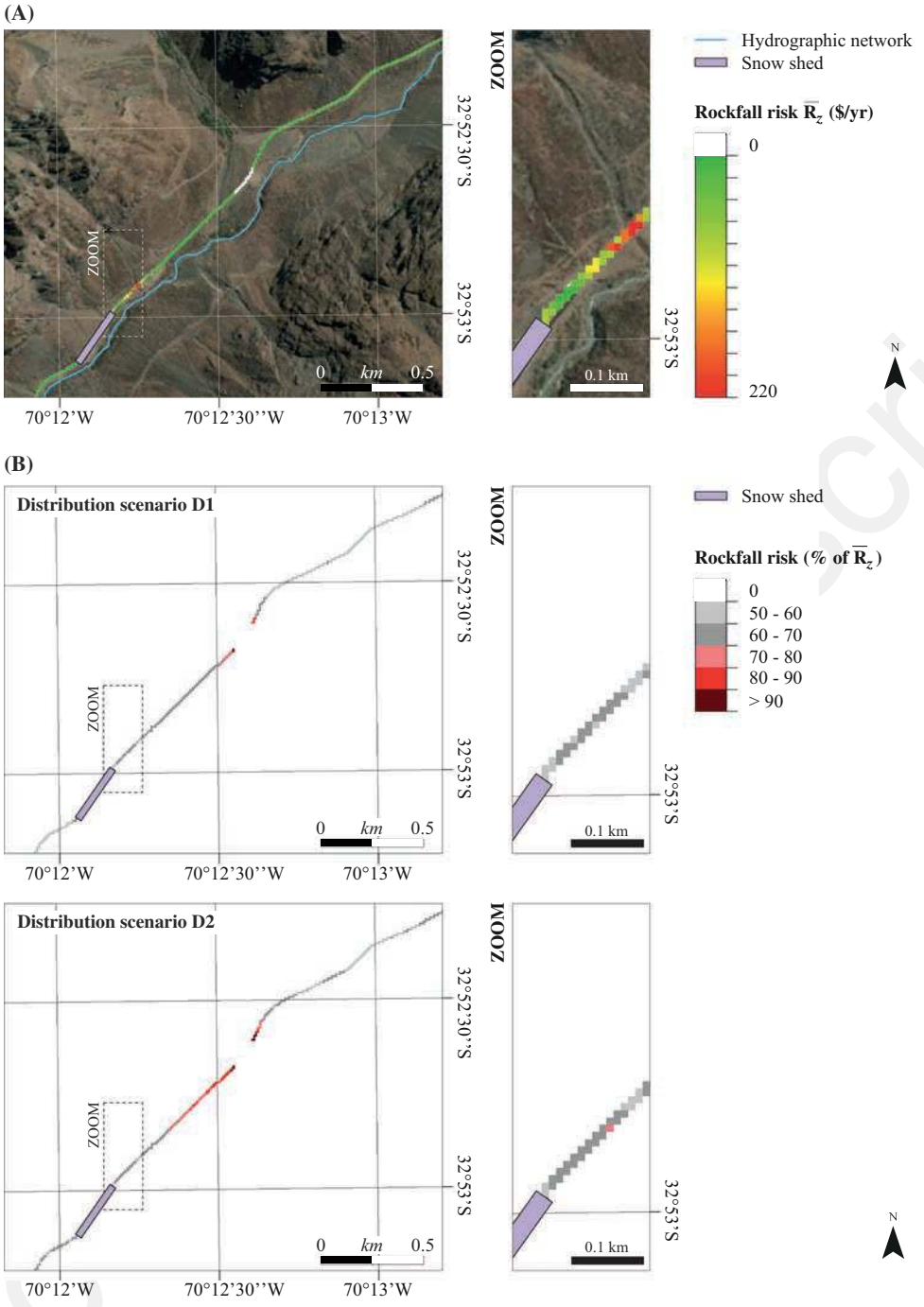

FIGURE 9 (A) Rockfall risk (i.e., annual expected cost in dollars) computed for road sections. Given the size of the site, the map focuses on the east of the toll (white square B in Figure 2A). Existing snow sheds and deflection structures are not considered in the analysis. The rockfall risk associated to this specific area, regardless of the vehicles, is equal to 5153 $/year. (B) Rockfall risk resulting from seismic events (% of the risk value $\overline{R}_z$) for rockfall volume distribution scenarios D1 and D2. The rockfall risk resulting from the volume distribution scenario D0 corresponds to 59% of $\overline{R}_z$ regardless the element at risk.

rate exceeds 0.002 fatalities/year (one fatality every 500 years) for six houses while it does not exceed 0.001 fatalities/years (one fatality every 1000 years) for all the remaining houses exposed to rockfalls. Sports centers and the toll were excluded from this calculation due to the difficulty in evaluating their occupation.

Finally, our results demonstrated that 0.028, 0.013, 0.010, and 0.143 vehicle accidents due to rockfalls are expected every years for cars, pickups, buses, and trucks, respectively. In that respect, a minimum of 0.195 fatalities are therefore expected every year along the road No. 60 (one fatality every 5 years). This value is a minimum estimate since the number

TABLE 4 Risk to people (i.e., number of fatalities per year) associated to the elements at risk in the Uspallata valley regardless triggering factors.

Risk to people (fatalities/years)	
Static elements	
Buildings	0.07
Hydroelectric plants	×
Road No. 60	
Cars	0.028
Pickups	0.013
Buses	0.010
Truck	0.143
Transandine railway	
Train	×
Total	0.265

of persons in each vehicle may be much higher than one. In other words, the mean number of fatalities per year expected at each 10 m at risk section is equal to 5^{-5}.

Overall, the minimum mean number of fatalities per year expected for people within houses and vehicles along the road No. 60 is therefore equal to 0.265. In other words, this value corresponds to one fatality every approximately 4 years. A detailed summary of the risk values for people is provided in Table 4.

5.4 | Seismically and meteorologically induced rockfall risk

Following Equation (17), risk values have been quantified for rockfalls triggered by ground motions (respectively, meteorological conditions) for our three volume distribution scenarios (Table 2). Rockfall risk resulting from seismic events for the rockfall volume distribution scenario D0 reaches 82,405 \$/year (59% of $\overline{R}_w$), and it is 57,546\$/year (41% of $\overline{R}_w$) for blocks triggered by meteorological events (Figure 10). In greater detail, under this distribution scenario, 59,137 \$/year of damage are expected every year on buildings from rockfall events released by earthquakes. Moreover, the rockfall risk expected on road No. 60 from earthquakes is 15,543 \$/year, against 10,855 \$/year from meteorological events. By considering scenario D1, the rockfall risk resulting from seismic and meteorological factors are equal to 84,604 \$/year (60% of $\overline{R}_w$) and 55,336\$/year (40% of $\overline{R}_w$), respectively (Figure 10). More specifically, the rockfall risk expected from earthquakes is 60,943 \$/year on buildings (Figure 8B) and 15,846 \$/year on road No. 60 (Figure 9B). Eventually, for the volume distribution scenario D2, the rockfall risk resulting from seismic events reaches 88,929 \$/year (64% of $\overline{R}_w$) against 51,040 \$/year (36% of $\overline{R}_w$) from meteorological events (Figure 10). In greater detail, 64,504 \$/year of damage are expected every year on buildings from rockfall events released by earthquakes (Figure 8B). Moreover, the rockfall risk expected on road No. 60 from earthquakes is 16,424

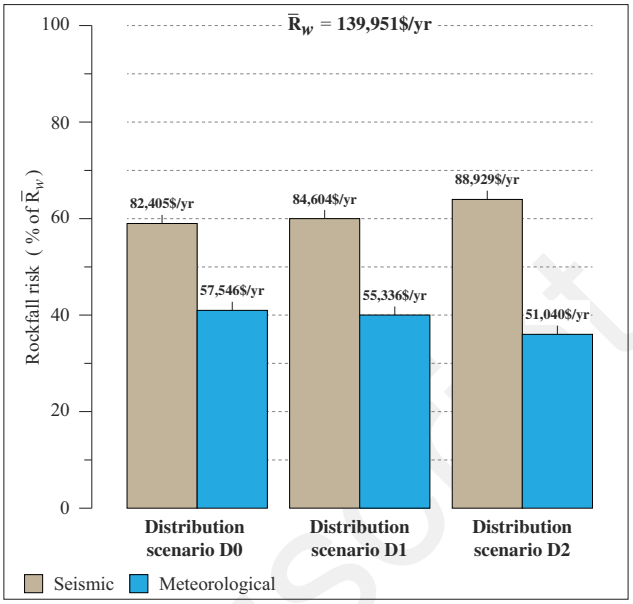

FIGURE 10 Rockfall risk (in \$/year and % of the total risk value $\overline{R}_w$) in the Uspallata valley for distribution scenarios D0, D1, and D2 representing different weighting among volume classes between seismic and meteorological triggered rockfall (Table 2, Figure 6).

\$/year (Figure 9B), against 9977 \$/year from meteorological events. A detailed summary of the risk values resulting from seismic and meteorological factors is provided in Table 5.

Overall, seismically and meteorologically induced rockfall risk estimates vary only slightly with volume distribution scenario. Indeed, seismically induced rockfall risk varies from 59% of $\overline{R}_w$ (82,405 \$/year) to 64% of $\overline{R}_w$ (88,929 \$/year) between "extreme" scenarios D0 and D2. Consequently, in this study, volume distributions as function of triggering factors do not significantly influence the respective weight of each rockfall driver in the total risk.

These results are largely robust to the choice of the GMM, with the exception of the Zhao et al. (2016) model where λ_{T_S} equals 5.06 events/year (Table C). In that latter case, seismically induced rockfall risk equals 58,919 \$/year (D0; 42% of $\overline{R}_w$), 60,492 \$/year (D1; 43% of $\overline{R}_w$), and 63,584 \$/year (D2; 45% of $\overline{R}_w$), so that meteorological triggers represent a larger portion of the total risk.

5.4.1 | Sensitivity to components

In order to quantify how rockfall risk is impacted by other uncertainties in its evaluation, the QRA procedure has been applied for alternative input variables, defined by increasing and decreasing the initial value by fixed percentages. Risk for the whole system w, buildings, and trucks has thus been calculated for each new input (leaving all other assumptions unchanged) and for three potential percentage errors of 5%, 10%, and 25%. All resulting risk estimates and comparison to default values are summarized in Table 6.

TABLE 5 Rockfall risk (i.e., annual expected cost in Dollars) associated to the elements at risk in the Uspallata valley (i) regardless triggering factors and (ii) as function of triggering factors for rockfall volume distribution scenarios D0, D1, and D2 (Table 2).

	Total	Dist. scenario D0		Dist. scenario D1		Dist. scenario D2	
		T_S	T_M	T_S	T_M	T_S	T_M
$\overline{R}_w$	139,951	82,405	57,546	84,604	55,336	88,929	51,040
Static elements							
Buildings	100,434	59,137	41,297	60,943	39,482	64,504	35,943
Hydroelectric plants	12,711.5	7485	5227	7573	5138	7756	4957
Road No. 60							
Cars	252	148	104	153	98	162	90
Pickups	148	87	61	90	58	95	53
Buses	2213	1303	910	1328	885	1376	837
Trucks	23,784	14,005	9780	14,274	9509	14,791	8997
Transandine railway							
Train	407	240	168	242	166	245	163

Regardless the elements at risk, rockfall risk increases/decreases linearly with the percentage of uncertainty allocated to Z_w and $\mathrm{Sim}_z(v_{Cl_i})$. For example, the total rockfall risk $\overline{R}_w$ varies from 139,951 \$/year to 146,949 \$/year (+5%), 153,946 \$/year (+10%), and 174,939 \$/year (+25%) for Z_w or $\mathrm{Sim}_z(v_{Cl_i})$ components increased by 5%, 10%, and 25%, respectively. Similarly, 5%, 10%, and 25% decreases in Z_w and $\mathrm{Sim}_z(v_{Cl_i})$ result in rockfall risk values of 132,953 \$/year (−5%), 125,956 \$/year (−10%), and 104,963 \$/year (−25%), respectively.

On the contrary, we can observe that variations within $l(z)$, ν_z or τ_z components have minor impacts on rockfall risk estimates. For example, a 25% increase in τ_z results in an $\overline{R}_w$ increase of 6% (from 139,951 \$/year to 148,348 \$/year). Yet, this is not true when focusing on rockfall risk for trucks where, for example, $\overline{R}_{trucks}$ increases from 23,784 \$/year to 31,633 \$/year (+33%) when decreasing by 25% the initial value of ν_z.

Regardless the elements at risk, important risk variations are also observed when varying the source surface R_s as well as reference period T_w. Indeed, a decrease of 25% in R_s or T_w rises $\overline{R}_{buildings}$ from 100,434 \$/year to 133,577 \$/year (+33%).

When focusing on the $\overline{d}_z(v_{Cl_i})$ component, we can observe that rockfall risk for buildings also decreases linearly with negative uncertainty percentages. In the opposite case, 5%, 10%, or 25% increases in $\overline{d}_z(v_{Cl_i})$ induce slight variations of the total rockfall risk. For example, $\overline{R}_{buildings}$ varies from 100,434 \$/year to 108,469 \$/year (+8%) when rising $\overline{d}_z(v_{Cl_i})$ by 25%.

Last, rockfall risk estimates have been evaluated for the GPD model 95% confidence interval. Regardless the elements at risk, variations in the rockfall volume distribution induce only slight impacts on rockfall risk estimates ($< \pm 5\%$).

6 | DISCUSSION, CONCLUSION, AND OUTLOOKS

6.1 | Main outcomes of the work

In this work, as an answer to the need for large-scale risk assessment methods coping for the numerous factors at play in vulnerable environments, we proposed a framework to perform holistic quantitative rockfall risk analyses potentially including a variety of infrastructure over large areas. Indeed, rockfall risk values were evaluated both in monetary terms and in terms of casualties, and at three different scales: (i) at individual level (i.e., individual structure and linear sections), (ii) by exposed element types (i.e., road, railway, hydroelectric power plants, buildings), and (iii) over the whole system at risk. This multiscale approach allows to address the risk from diverse perspectives, and (1) to precisely map the most risk-prone areas, (2) to identify the most at-risk units, and (3) to quantify the risk at the regional scale. Also, over large areas, cascading risks resulting from complex chains of processes may represent a large proportion of total risk. Our framework therefore combined models from different scientific disciplines in order to quantify seismically and meteorologically induced rockfall, and, ultimately, to separate total rockfall risk as function of its drivers. Hence, it is pioneering not only due to its unusually large-scale and Andean contexts, but also as it enables to quantify rockfall risk in regions where seismic activity is susceptible to produce considerable cascading effects, resulting in nonnegligible sources of loss amplifications.

Application was made to Uspallata valley, an archetypal valley of the Central Andes mountains where various elements at risk are attracted by strong economic interests and the strategic crossing between Chile and Argentina. We demonstrated that, in Uspallata, truck traffic as well as individual buildings were accounting for the largest proportion

TABLE 6 Sensitivity of rockfall risk (in $/year) for the whole system at risk w, buildings, and trucks to its components for ±5%, ±10%, ±25% changes with regard to their initial values.

	Z_w and $Sim_z(v_{Cl_i})$					
	+5%	**-5%**	**+10%**	**-10%**	**+25%**	**-25%**
$\overline{R}_w$(139,951)	+5% (146,949 $/yr)	−5% (132,953)	+10% (153,946)	−10% (125,956)	+25% (174,939)	−25% (104,963)
$\overline{R}_{buildings}$ (100,434)	+5% (105,456)	−5% (95,412)	+10% (110,477)	−10% (90,391)	+25% (125,542)	−25% (75,326)
$\overline{R}_{trucks}$ (23,784)	+5% (24,973)	−5% (22,595)	+10% (26,162)	−10% (21,406)	+25% (29,730)	−25% (17,838)
	$l(z)$					
	+5%	**−5%**	**+10%**	**−10%**	**+25%**	**−25%**
$\overline{R}_w$ (139,951)	+1% (141,351)	−1% (138,551)	+2% (142,750)	−2% (137,152)	+3% (144,150)	−3% (135,752)
$\overline{R}_{buildings}$ (100,434)	×	×	×	×	×	×
$\overline{R}_{trucks}$ (23,784)	+3% (24,498)	−3% (23,070)	+5% (24,973)	−5% (22,595)	+14% (27,114)	−14% (20,454)
	v_z					
	+5%	**−5%**	**+10%**	**−10%**	**+25%**	**−25%**
$\overline{R}_w$ (139,951)	−1% (138,551)	+1% (141,351)	−2% (137,152)	+2% (142,750)	−4% (134,353)	+6% (148,348)
$\overline{R}_{buildings}$ (100,434)	×	×	×	×	×	×
$\overline{R}_{trucks}$ (23,784)	−5% (22,595)	+5% (24,973)	−9% (21,643)	**+11%** (26,400)	−20% (19,027)	**+33%** (31,633)
	τ_z					
	+5%	**−5%**	**+10%**	**−10%**	**+25%**	**−25%**
$\overline{R}_w$ (139,951)	+1% (141,351)	−1% (138,551)	+2% (142,750)	−2% (137,152)	+6% (148,348)	−6% (131,554)
$\overline{R}_{buildings}$ (100,434)	×	×	×	×	×	×
$\overline{R}_{trucks}$ (23,784)	+5% (24,973)	−5% (22,595)	+10% (26,162)	−10% (21,406)	+25% (29,730)	−25% (17,838)
	R_s and T_w					
	+5%	**−5%**	**+10%**	**−10%**	**+25%**	**−25%**
$\overline{R}_w$ (139,951)	−5% (132,953)	+5% (146,949)	−9% (127,355)	**+11%** (155,346)	−20% (111,961)	**+33%** (186,135)
$\overline{R}_{buildings}$ (100,434)	−5% (95,412)	+5% (105,456)	−9% (91,395)	**+11%** (111,482)	−20% (80,347)	**+33%** (133,577)
$\overline{R}_{trucks}$ (23,784)	−5% (22,595)	+5% (24,973)	−9% (21,643)	**+11%** (26,400)	−20% (19,027)	**+33%** (31,633)
	$\overline{d}_z(v_{Cl_i})$					
	+5%	**−5%**	**+10%**	**−10%**	**+25%**	**−25%**
$\overline{R}_w$ (139,951)	+4% (145,549)	−4% (134,353)	+6% (148,348)	−7% (130,154)	+11% (155,346)	−20% (111,961)
$\overline{R}_{buildings}$ (100,434)	+3% (103,447)	−5% (95,412)	+5% (105,456)	−10% (90,391)	+8% (108,469)	−25% (75,326)
$\overline{R}_{trucks}$ (23,784)	×	×	×	×	×	×

of the total risk. Similarly, our results revealed that the total risk could amount several thousand dollars per year and reach high casualty rates, demonstrating the crucial need for a rigorous implementation of mitigation strategies in the future. Eventually, we highlighted the significant part of seismic activity in rockfall triggering and total risk. These results provide the basis for the prioritization of management and mitigation actions (Corominas et al., 2014) and demonstrate the applicability and usefulness of our approach for real case studies, notably in areas where high economic activity makes an in-depth knowledge and understanding of rockfall risk mandatory. In Uspallata, this is all the more true than rockfall risk that will increase in the future due to urban expansion, tourist development, and potential reinstallation of the Transandino railway (Moreiras, 2006). Our approach could therefore be applied with benefits in the future in many areas that share similar sensitivity to rockfall risk, and especially in regions where strong seismic activity is susceptible to produce considerable cascading effects.

6.2 | Pros and Cons of modeling assumptions

For the application case study, different shortcuts resulted from the large scale of the analysis. Given the large number of starting cells (191,780) within the studied domain, the number of rockfall simulations have been adjusted here to preserve data storage and processing (1900 simulations/starting cell). Furthermore, the interpolation of the DEM at a resolution of 10 m (which is already optimal given the scale of the studied area) did not enable to include small elements at risk (< 10 m). For example, our analysis could not account for penstock pipes carrying water to hydroelectric plants or transmission towers of electricity network.

Similarly, rockfall propagation is mainly determined by the topography, yet the limited resolution of the DEM (30×30 m) contributes to uncertainties when predicting trajectories. Fragmentation of rock blocks during propagation has also been neglected in this study, which somehow limits the realism of certain trajectory simulations. Even more critically, epistemic uncertainties related to the temporal occurrence of rockfalls and their associated volume distributions made risk assessment particularly difficult. For instance, the absence of historical catalog resulted in strong assumptions relating to the temporal window for the sampled blocks, leading to rough estimate of rockfall frequency. Similarly, the lack of knowledge regarding rockfall volume distribution as a function of the drivers required stringent assumptions to implement the QRA framework. Furthermore, the lack of precise information regarding traffic conditions (e.g., traffic jams) constrained us to assume the latter as uniformly distributed. Yet, traffic variations influence the temporal probability of a moving vehicle to encounter a block, which potentially affects final risk estimates.

Moreover, some uncertainties stem from the models themselves. Notably, results are very sensitive to Rockyfor3D parameterization, especially with regard to the soil properties and slope surface (Corona et al., 2017; Farvacque et al., 2019b). The choice of the models used to fit the volume frequency relationship or the physical vulnerability curve can also be questioned. Additionally, separation of total rockfall risk as a function of its drivers involved several models that inherently lead to numerous additional uncertainties. Indeed, seismically induced rockfall risk values should be considered cautiously as it is impossible to precisely evaluate the relevance of the Wilson and Keefer (1985) model as well as the number of individual blocks released at each seismic event exceeding the critical ground acceleration. Eventually, the choice of the GMM may affect the respective weight of each triggering factor in the temporal rate of occurrence of potentially damageable events (Table C), therefore impacting the proportion of each triggering factor in total risk.

All these limitations and uncertainty sources, as well as assumptions we made to cope with them should be kept in mind, especially when interpreting the risk estimates. However, we strongly believe that they do not hamper the interest of our methodological framework or even of the first large-scale risk values we provided for the case study. In practice, such assumptions are always mandatory for going from the overall risk problems formulation to its practical assessment (Corominas et al., 2005; Farvacque et al., 2019b). With regard to standard analyses, our approach is even more complex due to (i) the large-scale approach and (ii) the separation of rockfall risk as function of its drivers. Yet, we tried to make the most reasonable set of assumptions given the local knowledge, and keeping in mind that the computation should remain feasible, limiting the complexity of the models that could be used (e.g., we relied on a rather simple but robust and computationally efficient rockfall propagation model). Some shortcuts or uncertainties could be, in the future, rather easily levered by integrating additional data/knowledge and computational power within the same risk quantification framework. Notably refined mechanical models could be used locally for rockfall failure and propagation at specific hotspots of the studied areas and their results could be then hincasted at the scale of the entire study area. Also, new field studies could help refine some inputs regarding source areas and volume distributions. Eventually, note that we could already demonstrate the robustness of our results to one of the most critical assumptions as we could show that the volume distribution as a function of triggering factors does not significantly influence the respective weight of each rockfall driver in the total risk.

6.3 | Sensitivity of risk value to QRA components

The rockfall risk equation is associated to a large spectrum of parameters that remain difficult to precisely assess due to epistemic and aleatory uncertainties (Farvacque et al., 2019b; Wang et al., 2014). To our knowledge, in the field of rockfall, the impact of these uncertainties remain poorly studied (Wang et al., 2014) so that the weight of each component/parameter on the final risk estimates is widely misunderstood. By contrast, this study proposes a sensitivity analysis that aims to analyze how different values of the different risk components affect final risk estimates.

We observed that risk estimates are highly sensitive to the source surface R_s, the reference period T_w and the mean velocity of vehicle v_z. Indeed, slight decreases of these components induced rather large changes in risk estimates. On the contrary, risk estimates vary much less with changes in the remaining components, and, overall, obtained risk estimates appeared as rather robust to their specification. Yet, when focusing on specific elements at risk, they must be chosen with care. For example, we largely demonstrated the strong impact of mean velocity on final risk estimates for circulating elements at risk.

6.4 | Choice of the risk measure

Classically, risk from natural hazards (and for many other problems) is evaluated through the standard damage expectation, widely adopted since it is intuitive, and easy to compute, and to interpret. Indeed, given the linearity of this risk measure, risk for a whole system is simply the sum of individual risks for each element of the system. Yet, a major drawback lies in its inability to capture the whole range of consequences, especially those related to rare events. The expected damage therefore needs to be supplemented by other measures, as already proposed for rockfall risk in Farvacque et al. (2021) where rockfall risk is assessed at a municipality scale and for individual houses from financial risk measures (i.e., the value at risk and the expected shortfall).

In this study, we adopted one more time the expected damage, as a first step to deal with the complexity of our

risk system. However, further work should now complement our work with the evaluation of more advanced risk measures. In practice, this remains challenging as such risk measures require to evaluate the entire distribution of damages, accounting, for example, for dependencies between different rockfall events during the same earthquake, and/or cascading consequences of the same rockfall for different elements at risk. This is mandatory as for quantile-based risk measure, the risk for the whole system is no longer the sum of the risk for each element of the system. Yet, evaluating this entire damage distribution is a tremendous task for a large-scale and complex system as the one we studied in Uspallata, due to the numerous dependencies and nonlinear processes concerning hazards and/or damages involved. In addition, Farvacque et al. (2021) showed that even for single elements at risk, obtaining robust estimates of quantile-based risk measures is difficult for rockfall risk due to the highly nonlinear relation between hazard and damage (e.g., little damage or full destruction of a building for very close impact conditions). As a consequence, the work to be undertaken to provide quantile-based risk measures for a system at risk like ours remains huge, but it may be of great interest for enhancing knowledge on total risk and managing rockfall risk in an efficient and consistent way.

6.5 | Other outlooks for further work

Despite its holistic nature, our study considered costs and losses directly resulting from rockfall impacts and damages only. Yet, rockfall events can indirectly affect societies by disrupting utility services and critical infrastructures (blockage of transport lifelines, power outage, etc.). These indirect losses are generally hard to evaluate due to complex chains of cause–effects, but, arguably, they often represent a very significant part of total costs/losses. In that respect, our framework should in the future be expanded to include them within the QRA (potentially within quantile-based risk measures), in order to enhance the knowledge/assessment of rockfall risk and manage it in an even more efficient and consistent way, for instance, with risk measure alternative to the standard loss expectation. In Uspallata, this would be all the more important as: (i) alternative communication axes to cross the border are located hundreds of kilometers from Uspallata, thus generating important detours in case of road No. 60 closure; (ii) rockfall impacts on hydroelectric plants or transmission towers of electricity network could lead to a significant grid outage.

Eventually, our approach is clearly a step toward better inclusion of cascading effects within quantitative risk assessment, but only a first step. The necessary inclusion of further knowledge regarding seismic triggers within the framework has already been mentioned. Also, the framework could be extended to more than two trigger types. Eventually, and even more widely, the approach could be transferred to a wide range of natural hazards, such as landslide or flooding, as a contribution to the necessary development of new methods accounting for multihazards and cascading risks in a consistent way (Curt, 2021; Zuccaro et al., 2018). This would contribute to a better understanding of complex chains of processes, and would be useful for the development and coordination of mitigation strategies integrating multiple hazardous events acting and cascading over the same vulnerable territories.

ACKNOWLEDGMENTS

This research was financially supported by a grant from LabEx OSUG@2020 (Investissements d'avenir - ANR10 LABX56), the ECOS-Sud project (Programme de coopération ECOS SudCONICYT - Chile), a Ph.D. grand from Rhône-Alpes Region - ARC Environnement 3, and the French National Research Agency in the Investissements d'Avenir program (ANR-15-IDEX-02) within the cross-disciplinary Risk@Univ. Grenoble Alpes program. For the French and Chilean exchanges, it has benefited from the support of the Chilean National Research Center for Integrated Natural Disaster Management (ANID-CIGIDEN 15110017) and from the French National Research Agency through the Statistical Modelling for the Assessment and mitigation of mountain Risks in a changing Environment—SMARTEN program (ANR- 20-Tremplin-ERC8-0001). IGE/INRAE is member of Labex OSUG. Also, Dr. Candia has received financial support from Facultad de Ingeniería at Universidad del Desarrollo, Chile.

ORCID

Manon Farvacque https://orcid.org/0000-0003-1831-4713

REFERENCES

Abrahamson, N. A., & Gulerce, Z. (2022). Summary of the Abrahamson and Gulerce NGA-SUB ground-motion model for subduction earthquakes. *Earthquake Spectra*, *38*(4), 2638–2681.

AghaKouchak, A., Huning, L. S., Chiang, F., Sadegh, M., Vahedifard, F., Mazdiyasni, O., Moftakhari, H., & Mallakpour, I. (2018). How do natural hazards cascade to cause disasters? *Nature*, *561*(7724), 458–460.

Agliardi, F., Crosta, G. B., & Frattini, P. (2009). Integrating rockfall risk assessment and countermeasure design by 3d modelling techniques. *Natural Hazards and Earth System Science*, *9*(4), 1059–1073.

Aven, T. (2009). Risk analysis and management. Basic concepts and principles. *Reliability: Theory & Applications*, *4*(1 (12)), 57–73.

Bourrier, F., Baroth, J., & Lambert, S. (2016). Accounting for the variability of rock detachment conditions in designing rockfall protection structures. *Natural Hazards*, *81*(1), 365–385.

Budetta, P., De Luca, C., & Nappi, M. (2016). Quantitative rockfall risk assessment for an important road by means of the rockfall risk management (ro.ma.) method. *Bulletin of Engineering Geology and the Environment*, *75*(4), 1377–1397.

Bunce, C. M., Cruden, D. M., & Morgenstern, N. R. (1997). Assessment of the hazard from rock fall on a highway. *Canadian Geotechnical Journal*, *34*(3), 344–356.

Candia, G., De Pascale, G., Montalva, G., & Ledezma, C. (2016). *Geotechnical reconnaissance of the 2015 Illapel earthquake*. Geotechnical Extreme Events Reconnaissance (GEER) Association. Report No. GEER-043.

Candia, G., Macedo, J., Jaimes, M. A., & Magna-Verdugo, C. (2019). A new state-of-the-art platform for probabilistic and deterministic seismic hazard assessment. *Seismological Research Letters*, *90*(6), 2262–2275.

Cappabianca, F., Barbolini, M., & Natale, L. (2008). Snow avalanche risk assessment and mapping: A new method based on a combination of

statistical analysis, avalanche dynamics simulation and empirically-based vulnerability relations integrated in a GIS platform. *Cold Regions Science and Technology*, *54*(3), 193–205.

Coles, S. (2001). *An introduction to statistical modeling of extreme values*. *Springer series in statistics*. Springer.

Corominas, J., Copons, R., Moya, J., Vilaplana, J. M., Altimir, J., & Amigó, J. (2005). Quantitative assessment of the residual risk in a rockfall protected area. *Landslides*, *2*(4), 343–357.

Corominas, J., Matas, G., & Ruiz-Carulla, R. (2019). Quantitative analysis of risk from fragmental rockfalls. *Landslides*, *16*(1), 5–21.

Corominas, J., & Mavrouli, O. (2013). Rockfall quantitative risk assessment. In S. Lambert & F. Nicot (Eds.), *Rockfall engineering* (pp. 255–301). John Wiley & Sons, Inc.

Corominas, J., van Westen, C., Frattini, P., Cascini, L., Malet, J.-P., Fotopoulou, S., Catani, F., Van Den Eeckhaut, M., Mavrouli, O., Agliardi, F., Pitilakis, K., Winter, M. G., Pastor, M., Ferlisi, S., Tofani, V., Hervás, J., & Smith, J. T. (2014). Recommendations for the quantitative analysis of landslide risk. *Bulletin of Engineering Geology and the Environment*, *73*, 209–263.

Corona, C., Lopez-Saez, J., Favillier, A., Mainieri, R., Eckert, N., Trappmann, D., Stoffel, M., Bourrier, F., & Berger, F. (2017). Modeling rockfall frequency and bounce height from three-dimensional simulation process models and growth disturbances in submontane broadleaved trees. *Geomorphology*, *281*, 66–77.

Corona, C., Trappmann, D., & Stoffel, M. (2013). Parameterization of rockfall source areas and magnitudes with ecological recorders: When disturbances in trees serve the calibration and validation of simulation runs. *Geomorphology*, *202*, 33–42.

Crosta, G. B., & Agliardi, F. (2003). A methodology for physically based rockfall hazard assessment. *Natural Hazards and Earth System Science*, *3*(5), 407–422.

Curt, C. (2021). Multirisk: What trends in recent works? A bibliometric analysis. *Science of The Total Environment*, *763*, 142951.

D'Amato, J., Hantz, D., Guerin, A., Jaboyedoff, M., Baillet, L., & Mariscal, A. (2016). Influence of meteorological factors on rockfall occurrence in a middle mountain limestone cliff. *Natural Hazards and Earth System Sciences*, *16*(3), 719–735.

DeRoin, N., & McNutt, S. R. (2012). Rockfalls at Augustine Volcano, Alaska: The influence of eruption precursors and seasonal factors on occurrence patterns 1997-2009. *Journal of Volcanology and Geothermal Research*, *211-212*, 61–75.

Dorren, L. (2012). *Rockyfor3d (v5.1) revealed—Transparent description of the complete 3d rockfall model*. ecorisQ paper, 32.

Dorren, L. K., Berger, F., le Hir, C., Mermin, E., & Tardif, P. (2005). Mechanisms, effects and management implications of rockfall in forests. *Forest Ecology and Management*, *215*(1-3), 183–195.

Eckert, N., & Giacona, F. (2023). Towards a holistic paradigm for long-term snow avalanche risk assessment and mitigation. *Ambio*, *52*, 711–732.

Eckert, N., Keylock, C., Bertrand, D., Parent, E., Faug, T., Favier, P., & Naaim, M. (2012). Quantitative risk and optimal design approaches in the snow avalanche field: Review and extensions. *Cold Regions Science and Technology*, *79-80*, 1–19.

Farvacque, M., Eckert, N., Bourrier, F., Corona, C., Lopez-Saez, J., & Toe, D. (2020). Évaluation quantitative du risque rocheux: de la formalisation à l'application sur les zones urbanisées ou urbanisables. *Revue française de Géotechnique*, *163*, 7.

Farvacque, M., Eckert, N., Bourrier, F., Corona, C., Lopez-Saez, J., & Toe, D. (2021). Quantile-based individual risk measures for rockfall-prone areas. *International Journal of Disaster Risk Reduction*, *53*, 10 1932.

Farvacque, M., Lopez-Saez, J., Corona, C., Toe, D., Bourrier, F., & Eckert, N. (2019a). How is rockfall risk impacted by land-use and land-cover changes? Insights from the French Alps. *Global and Planetary Change*, *174*, 138–152.

Farvacque, M., Lopez-Saez, J., Corona, C., Toe, D., Bourrier, F., & Eckert, N. (2019b). Quantitative risk assessment in a rockfall-prone area: the case study of the Crolles municipality (Massif de la Chartreuse, French Alps). *Géomorphologie: Relief, Processus, Environment*, *25*(1), 7–19.

Favier, P., Bertrand, D., Eckert, N., & Naaim, M. (2014). A reliability assessment of physical vulnerability of reinforced concrete walls loaded by snow avalanches. *Natural Hazards and Earth System Sciences*, *14*, 689–704.

Favier, P., Bertrand, D., Eckert, N., Ousset, I., & Naaim, M. (2018). Assessing fragility of a reinforced concrete element to snow avalanches using a non-linear dynamic mass-spring model. *Natural Hazards and Earth System Sciences*, *18*(9), 2507–2524.

Feng, L., Pazzi, V., Intrieri, E., Gracchi, T., & Gigli, G. (2019). Rockfall seismic features analysis based on in situ tests: Frequency, amplitude, and duration. *Journal of Mountain Science*, *16*(5), 955–970.

Ferrari, F., Giacomini, A., & Thoeni, K. (2016). Qualitative rockfall hazard assessment: A comprehensive review of current practices. *Rock Mechanics and Rock Engineering*, *49*(7), 2865–2922.

Fifer, J. V. (1991). *United States perceptions of Latin America, 1850-1930: a New West south of Capricorn?* Manchester University Press; Distributed exclusively in the USA by St. Martin's Press.

Fifer, V. (1994). Andes crossing: Old tracks and new opportunities at the Uspallata Pass. *Yearbook. Conference of Latin Americanist Geographers*, *20*, 35–48.

Frattini, P., Crosta, G., Carrara, A., & Agliardi, F. (2008). Assessment of rockfall susceptibility by integrating statistical and physically-based approaches. *Geomorphology*, *94*(3-4), 419–437.

Guzzetti, F., Reichenbach, P., & Ghigi, S. (2004). Rockfall hazard and risk assessment along a transportation corridor in the Nera valley, central Italy. *Environmental Management*, *34*(2), 191–208.

Guzzetti, F., Reichenbach, P., & Wieczorek, G. F. (2003). Rockfall hazard and risk assessment in the Yosemite Valley, California, USA. *Natural Hazards and Earth System Science*, *3*(6), 491–503.

Hayes, G. P., Wald, D. J., & Johnson, R. L. (2012). Slab1.0: A three-dimensional model of global subduction zone geometries: SLAB1.0 3d subduction geometry. *Journal of Geophysical Research: Solid Earth*, *117*(B1), B01302.

HAZUS. (2003). *Multi-hazard loss estimation methodology, earthquake model, HAZUS MH 2.1, technical manual*. Developed by the Department of Homeland Security, Federal Emergency Management Agency, Mitigation Division, Washington, D.C.

Kanari, M., Katz, O., Weinberger, R., Porat, N., & Marco, S. (2019). Evaluating earthquake-induced rockfall hazard near the Dead Sea Transform. *Natural Hazards and Earth System Sciences*, *19*(4), 889–906.

Kaplan, S., & Garrick, B. J. (1981). On the quantitative definition of risk. *Risk Analysis*, *1*(1), 11–27.

Karlsson, P.-O., & Haimes, Y. Y. (1988). Risk-based analysis of extreme events. *Water Resources Research*, *24*(1), 9–20.

Kuehn, N., Bozorgnia, Y., Campbell, K., & Gregor, N. (2020). Partially non-ergodic ground-motion model for subduction regions using the NGA subduction database. PEER Reports, Pacific Earthquake Engineering Research Center, University of California, Berkeley, CA. Series.

Lambert, S. (Ed.). (2011). *Rockfall engineering*. ISTE, London. OCLC: 774358397.

Li, X.-n., Ling, S.-x., Sun, C.-w., Xu, J.-x., & Huang, T. (2019). Integrated rockfall hazard and risk assessment along highways: An example for Jiuzhaigou area after the 2017 Ms 7.0 Jiuzhaigou earthquake, China. *Journal of Mountain Science*, *16*(6), 1318–1335.

Loye, A., Jaboyedoff, M., & Pedrazzini, A. (2009). Identification of potential rockfall source areas at a regional scale using a DEM-based geomorphometric analysis. *Natural Hazards and Earth System Science*, *9*(5), 1643–1653.

Macciotta, R., Martin, C. D., & Cruden, D. M. (2015). Probabilistic estimation of rockfall height and kinetic energy based on a three-dimensional trajectory model and Monte Carlo simulation. *Landslides*, *12*(4), 757–772.

Marzorati, S., Luzi, L., & De Amicis, M. (2002). Rock falls induced by earthquakes: a statistical approach. *Soil Dynamics and Earthquake Engineering*, *22*(7), 565–577.

Mavrouli, O., & Corominas, J. (2010). Rockfall vulnerability assessment for reinforced concrete buildings. *Natural Hazards and Earth System Science*, *10*(10), 2055–2066.

Mavrouli, O., & Corominas, J. (2018). TXT-tool 4.034-1.1: Quantitative rockfall risk assessment for roadways and railways. In K. Sassa, B. Tiwari, K.-F. Liu, M. McSaveney, A. Strom, & H. Setiawan (Eds.), *Landslide dynamics: ISDR-ICL landslide interactive teaching tools* (pp. 509–519). Springer International Publishing.

Melching, C. S., & Pilon, P. J. (1999). *Comprehensive risk assessment for natural hazards*. World Meteorological Organization, WMO/TD, Geneva.

Michoud, C., Derron, M.-H., Horton, P., Jaboyedoff, M., Baillifard, F.-J., Loye, A., Nicolet, P., Pedrazzini, A., & Queyrel, A. (2012). Rockfall hazard and risk assessments along roads at a regional scale: Example in Swiss Alps. *Natural Hazards and Earth System Science*, *12*(3), 615–629.

Montalva, G. A., Bastías, N., & Rodriguez-Marek, A. (2017). Ground-motion prediction equation for the Chilean subduction zone. *Bulletin of the Seismological Society of America*, *107*(2), 901–911.

Moos, C., Fehlmann, M., Trappmann, D., Stoffel, M., & Dorren, L. (2017). Integrating the mitigating effect of forests into quantitative rockfall risk analysis—Two case studies in Switzerland. *International Journal of Disaster Risk Reduction*, *32*, 55–74.

Moreiras, S. M. (2006). Frequency of debris flows and rockfall along the Mendoza river valley (Central Andes), Argentina: Associated risk and future scenario. *Quaternary International*, *158*(1), 110–121.

Parker, G. A., Stewart, J. P., Boore, D. M., Atkinson, G. M., & Hassani, B. (2022). NGA-subduction global ground motion models with regional adjustment factors. *Earthquake Spectra*, *38*(1), 456–493.

Pickands, J. (1975). Statistical inference using extreme order statistics. *The Annals of Statistics*, *3*(1), 119–131.

Poulos, A., Monsalve, M., Zamora, N., & de la Llera, J. C. (2019). An updated recurrence model for Chilean subduction seismicity and statistical validation of its Poisson nature. *Bulletin of the Seismological Society of America*, *109*(1), 66–74.

Pörtner, O., Roberts, D., Masson-Delmotte, V., Zhai, P., Tignor, M., Poloczanska, E., Mintenbeck, K., Nicolai, M., Okem, A., Petzold, J., Rama, B., & Weyer, N. (Eds.) (2019). *IPCC special report on the ocean and cryosphere in a changing climate*. IPCC.

Purcell, H. (2007). *Portillo: el espíritu de los Andes = The spirit of the Andes*. Aguilar Chilena.

Sernageomin. (2003). *Geologic map of Chile: Digital version, scale 1:1.000.000, Santiago, Chile*. https://www.sernageomin.cl/

Serre, D., & Heinzlef, C. (2018). Assessing and mapping urban resilience to floods with respect to cascading effects through critical infrastructure networks. *International Journal of Disaster Risk Reduction*, *30*, 235–243.

Stoffel, M., Ballesteros Cánovas, J. A., Luckman, B. H., Casteller, A., & Villalba, R. (2019). Tree-ring correlations suggest links between moderate earthquakes and distant rockfalls in the Patagonian Cordillera. *Scientific Reports*, *9*(1), 12112.

Strunden, J., Ehlers, T. A., Brehm, D., & Nettesheim, M. (2015). Spatial and temporal variations in rockfall determined from TLS measurements in a deglaciated valley, Switzerland: Rockfall in a deglaciated valley. *Journal of Geophysical Research: Earth Surface*, *120*(7), 1251–1273.

Toppe, R. (1987). Terrain models—A tool for natural hazard mapping. In B. Salm & H. Gubler (Eds.), *Avalanche formation, movement and effects* (Vol. 162, pp. 629–638). International Association of Hydrological Sciences.

Unterrader, S., Almond, P., & Fuchs, S. (2018). Rockfall in the Port Hills of Christchurch: Seismic and non-seismic fatality risk on roads: Rockfall fatality risks in the Port Hills. *New Zealand Geographer*, *74*(1), 3–14.

Volkwein, A., Schellenberg, K., Labiouse, V., Agliardi, F., Berger, F., Bourrier, F., Dorren, L. K. A., Gerber, W., & Jaboyedoff, M. (2011). Rockfall characterisation and structural protection—A review. *Natural Hazards and Earth System Science*, *11*(9), 2617–2651.

Wang, S., Hong, L., Chen, X., Zhang, J., & Yan, Y. (2011). Review of interdependent infrastructure systems vulnerability analysis. In *2011 2nd international conference on intelligent control and information processing* (pp. 446–451). Harbin, China: IEEE.

Wang, X., Frattini, P., Crosta, G. B., Zhang, L., Agliardi, F., Lari, S., & Yang, Z. (2014). Uncertainty assessment in quantitative rockfall risk assessment. *Landslides*, *11*(4), 711–722.

Wilson, R. C., & Keefer, D. K. (1985). Predicting areal limits of earthquake-induced landsliding. In *Evaluating earthquake hazards in the Los Angeles Region: an Earth science perspective., USGS Professional Paper 1360* (pp. 317–345). US Geological Survey, 1985.

Yoshikawa, H., & Goda, K. (2014). Financial seismic risk analysis of building portfolios. *Natural Hazards Review*, *15*(2), 112–120.

Zhao, J. X., Jiang, F., Shi, P., Xing, H., Huang, H., Hou, R., Zhang, Y., Yu, P., Lan, X., Rhoades, D. A., Somerville, P. G., Irikura, K., & Fukushima, Y. (2016). Ground-motion prediction equations for subduction slab earthquakes in Japan using site class and simple geometric attenuation functions. *Bulletin of the Seismological Society of America*, *106*(4), 1535–1551.

Zimmerman, R., & Restrepo, C. E. (2009). Analyzing cascading effects within infrastructure sectors for consequence reduction. In *2009 IEEE conference on technologies for homeland security* (pp. 165–170). MA, USA: IEEE.

Zuccaro, G., De Gregorio, D., & Leone, M. F. (2018). Theoretical model for cascading effects analyses. *International Journal of Disaster Risk Reduction*, *30*, 199–215.

APPENDIX A

Landslide susceptibility category (from None to X) assigned as a function of geologic group, groundwater conditions, and slope angle (HAZUS, 2003).

	Slope angle (degrees)					
Geological group	**0–10**	**10–15**	**15–20**	**20–30**	**30–40**	**> 40**
	Groundwater condition: dry					
Strongly cemented rocks	None	None	I	II	IV	VI
Weakly cemented rocks	None	III	IV	V	VI	VII
Argillaceous rocks	V	VI	VII	IX	IX	IX
	Groundwater condition: wet					
Strongly cemented rocks	None	III	VI	VII	VIII	VIII
Weakly cemented rocks	V	VIII	IX	IX	IX	X
Argillaceous rocks	VII	IX	X	X	X	X

APPENDIX B

Critical accelerations (A_c) for landslide susceptibility categories (HAZUS, 2003).

Susceptibility category	**None**	**I**	**II**	**III**	**IV**	**V**	**VI**	**VII**	**VIII**	**IX**	**X**
Critical acceleration (g)	None	0.60	0.50	0.40	0.35	0.30	0.25	0.20	0.15	0.10	0.05

APPENDIX C

Rockfall frequency for seismic (λ_{T_S}) and meteorological (λ_{T_M}) triggers given five alternative GMMs. The table provides the respective weight of each triggering factor in the temporal rate of occurrence of potentially damageable events (λ) for five alternative GMMs. In that respect, we can consider the potential variability of PGA values in the seismically induced rockfall risk. As a reminder, the initial values obtained in this study (Section 3.3.1) correspond to 7 events/year (λ_{T_S}, 59% of λ) and 5 events/year (λ_{T_M}, 41% of λ).

Ground motion model	λ_{T_S} **(events/year)**	λ_{T_M} **(events/year)**
Zhao et al. (2016)	5.06 (42% of λ)	6.97 (58% of λ)
Montalva et al. (2017)	6.36 (53% of λ)	5.67 (47% of λ)
Kuehn et al. (2020)	7.49 (62% of λ)	4.54 (38% of λ)
Parker et al. (2022)	9.29 (77% of λ)	2.74 (23% of λ)
Abrahamson and Gulerce (2022)	7.54 (63% of λ)	4.49 (37% of λ)

APPENDIX D

Rockfall volume probabilities in volume classes as function of triggering factors: The rockfall volume probability in the volume class v_{Cl} for seismic triggered rockfall (T_S) is given by:

$$\Pr^{T_S}(v_{Cl}) = \frac{\lambda \times \Pr(v_{Cl}) - \Pr^{T_M}(v_{Cl}) \times \lambda_{T_M}}{\lambda_{T_S}}, \qquad (D.1)$$

where λ is the frequency of rockfall events (12 events/year; Section 4.2.1) and $\Pr(v_{Cl})$ the rockfall volume probability in the volume class v_{Cl} (Section 4.3; Figure 5). λ_{T_S} (7 events/year; Section 4.2.2) and λ_{T_M} (5 events/year; Section 4.2.2) correspond to the rockfall frequency for seismic and meteorological triggers, respectively. $\Pr^{T_M}(v_{Cl})$ is the rockfall volume probability in the volume class v_{Cl} for meteorological triggers and is assigned in this study by the author respecting $\sum_{j=1}^{n} \Pr^{T_M}(v_{Cl_i}) = 1$.